ADAPTIVE GEOMETRY TRANSFORMATION AND REPAIR METHODOLOGY FOR HYBRID MANUFACTURING

A Thesis
Presented to
The Academic Faculty

by

Maxwell Praniewicz

In Partial Fulfillment
of the Requirements for the Degree
Master of Science in the
School of Mechanical Engineering

Georgia Institute of Technology
August 2018

ADAPTIVE GEOMETRY TRANSFORMATION AND REPAIR METHODOLOGY FOR HYBRID MANUFACTURING

Approved by:

Dr. Christopher Saldana, Advisor
School of Mechanical Engineering
Georgia Institute of Technology

Dr. Thomas Kurfess
School of Mechanical Engineering
Georgia Institute of Technology

Dr. Shreyes Melkote
School of Mechanical Engineering
Georgia Institute of Technology

Date Approved: May 04, 2018

ACKNOWLEDGEMENTS

I first would like to thank my committee members Dr. Kurfess and Dr. Melkote for their time and commitment. I especially would like to thank my advisor, Dr. Christopher Saldana, for his guidance, understanding, and insight. I would also like to thank Delta Airlines for their support and technical insight on this project. Additionally, I would like to thank my fellow labmates, PMRC students, and everyone in the Montgomery Machining Mall for any and all assistance they provided me throughout this project. Lastly, I would like to thank my family and Jess for all their encouragement and support; without you all, I would not be here.

TABLE OF CONTENTS

LIST OF TABLES

LIST OF FIGURES

SUMMARY

With hybrid manufacturing maturing into a commercial scale, industries are pushing to integrate and fully utilize this new technology in their production facilities. Using the capability to interleave additive and subtractive manufacturing, these systems provide an opportunity to perform component repair through additive material deposition and resurfacing via machining. This is particularly attractive to industries which utilize complex, often freeform, components which require a large capital investment, such as the aerospace and mold and die industries. However, in service these components may experience unique distortions or wear, and therefore each require a unique repair strategy. This work seeks to create an adaptive transformation method for part geometry, which can adapt the process to match the needs of an individual component within the context of a commercial hybrid manufacturing system using currently available on machine inspection technology; greatly improving the efficiency of repair processes. To accomplish this, a new methodology for the adaptation of a nominal CAD geometry to a component is presented which combines data registration and reverse engineering strategies for aero engine components. The accuracy of this deformation method is first examined, then simulations are completed to explore the potential efficiency gains in both the additive and subtractive phases of a hybrid repair process.

CHAPTER 1. INTRODUCTION

Due to significant cost for initial manufacture, re-manufacture and repair is common practice for a number of components used in commercial airliners. These re-manufacturing processes are the backbone of the economic viability of the commercial airline industry, as significant cost savings are seen in repair. However, the repair of engine components, such as compressor blades, possess a difficult challenge in re-manufacturing. Throughout their lifecycle, these components experience erosion and wear. However, due to other deformation which occur in the blade geometry on a part by part basis, these components cannot be repaired using a single predetermined repair strategy. Instead, this repair process must be adapted on a part by part basis to conform to the unique geometry of each component. The current geometric condition of the part must first be captured. Then, this actual data must be used in conjuncture with the nominal geometry for the component to create an adapted model. Rigid data registration techniques can be used to align these two differential data sets, but this does not account for deformation which may occur in the data collected from the actual component. Non-rigid registration techniques are present in the literature; however these methods often include time consuming evaluation of global cost functions to minimize error, making them impractical for on-line implementation in a manufacturing process. The field of reverse engineering and inspection of airfoil geometries has developed unique methods for detection and correction of deformations through the use of parameterized models. These techniques, if combined with rigid registration, could prove useful in construction of geometry for adaptive repair processes.

Furthermore, in present literature the inspection, deposition, and blending phases of the repair process are often treated individually and do not operate in connection with one another. Hybrid manufacturing systems, which combine additive deposition of material and high accuracy CNC machining could be used in conjunction with adaptive process planning strategies to localize the entire repair process to one machine. While the combination of these processes to one machine has been demonstrated previously in the literature, it requires purpose-built machines to do so. Newly released commercial hybrid manufacturing systems provide an opportunity for re-manufacturers to develop their own localized repair processes without the commitment of a dedicated machine.

This work seeks to develop an adaptive model transformation technique for the re-manufacture of components which are often deformed or distorted in normal operation within the framework of a commercially available hybrid manufacturing system. The method described combines data registration and techniques utilized in the definition and reconstruction of airfoil profiles to adapt the geometry. The adaptation of airfoil geometries is used as an example throughout this work and are used to evaluate the quality of the adaptation to various levels of deformation. However, this method can be applied to any geometry which can be defined as a thickness distribution about a mean line. Furthermore, this study also examines the applicability of the developed method within a hybrid manufacturing framework. Simulations are conducted which evaluate the efficiency of geometry adaptation in the deposition repair process as compared to a current industry practice. However, the subsequent machining strategy is also affected by the choice of deposition strategy. Therefore, machining simulations are performed to evaluate this impact, utilizing adaptive toolpath strategies.

1.1 Problem statement

Adaptive repair methods for high value components are critical techniques that can exploit recent advances in hybrid additive and subtractive manufacturing processes. While some methods have been proposed and evaluated to provide for repair of worn part geometries, no methods currently are available for adaptive repair of part geometries in situations wherein the original part model geometry is not fully established, such as in the case of third party repair configurations. The purpose of this work is to develop an adaptive registration method for the repair of high valued components, which is capable of execution within the framework of a commercial hybrid manufacturing system. This method should be able to accurately align and deform a nominal model to match the geometry of a component to be repaired. The presented work develops an adaptive registration method for this purpose, demonstrates its capabilities and exhibits the potential gains if adopted.

1.2 Thesis organization

This thesis document is organized into the following sections: introduction, background, methodology, results and discussion, and conclusion. Chapter 2 provides a brief review of the current state of hybrid manufacturing systems, an examination of developed registration techniques, and a summary of techniques used in the characterization and reverse engineering of airfoil geometries. Chapter 3 provides a detailed explanation of the adaptive registration method developed. Chapter 4 presents the results of registration accuracy studies and simulation of potential impact, as well as discussion regarding these. Chapter 5 presents the key findings and contributions from this work and recommendations of future research in this topic.

CHAPTER 2. BACKGROUND

This chapter reviews several areas of research pertinent to this work including hybrid manufacturing, data registration techniques, and reverse engineering techniques. This chapter begins with and overview of hybrid manufacturing, describing the motivation for the localization and combination of additive and subtractive manufacturing processes and reviewing the current state of hybrid manufacturing technology. Next, this chapter discusses various data registration techniques, including detailed explanations of the most commonly used methods. The chapter then concludes by exploring techniques used the in the digitization and reverse engineering of aero-engine components.

2.1 Hybrid manufacturing

While additive manufacturing (AM) processes allow for the easy creation of complex freeform surfaces, lattice structures, and internal geometries, they are often not methods capable of producing functional components in isolation. Post-processing is often required to bring the component to the desired final state of the manufacturer. However, the finishing processes implemented may vary depending on final requirements of the part. Components produced by powder based processes often have higher surface roughness due to the adhesion of particles which do not entirely melt, but fuse to the hot substrate [1]. Often, due to the layer-wise nature of AM processes, the final surface roughness will not be uniform throughout the component, and differences exist in quality of vertical, angled and flat surfaces [2, 3]. Surface roughness and quality of these components is often corrected by mechanical surface treatment processes after completion such as polishing or shot peening [4].

Final component accuracy is also a common constraint for components produced via AM. Due to the layer-based deposition strategy, aliasing error is expected in the production of curved surfaces. Methods to decrease geometric inaccuracies resulting from this "staircase effect" are an ongoing area of research and include altering build orientation and differential layer shape to reduce this effect [5, 6]. Residual stress resulting from the deposition process can also contribute to geometric errors, making final part accuracy difficult to estimate [7, 8]. However, the effects of residual stresses can be mitigated for most materials using different heat-treating techniques [9, 10]. Machining is often used as a secondary process to AM and can be used in order to bring to the component to final geometric qualification specifications or even simply separate the component from a build plate used in the additive manufacturing process [11-14]. Not only does each post processing step add additional cost and manufacturing time, but each step also includes significant time to transfer and setup the part between these steps. These post processing steps end up being a large contribution to the final cost of a part produced by AM [15].

Hybrid manufacturing systems attempt to reduce these transfers and potential setup issues by combining AM processes with conventional subtractive processes in a single machine. This allows the machine to switch modalities between adding and subtracting material at any point in the overall manufacturing process. This interleaving of different manufacturing techniques allows the process to maximize the benefits of each individual method and allows for the creation of components that could not be achieved by use of either individual method in isolation, often referred to as the concept of "1+1=3" [16].

These systems have the capability to produce components with complex or internal geometries with acceptable surface quality [17, 18]. Further, this allows for the rapid creation of components otherwise prohibitively expensive to manufacture in small quantities [19]. These processes also allow for the creation of small features on components that otherwise would require excessive material removal to create via subtractive processes such as flanges, fins, or bosses [20]. Since these machines are capable of switching between either adding or subtracting material at any point in the manufacture of a component, optimal sequencing of the overall additive/subtractive build process is a substantially more complex problem than in a single function modality framework. This has prompted research in the planning and sequencing of these hybrid strategies [21, 22].

Hybrid manufacturing systems provide the unique capability of performing component repair on worn performance components in a single machine setup. Through material buildup by additive material deposition and resurfacing by machining, worn or damaged components can be refurbished to usable conditions. Ideal candidates for repair are components which are unlikely to be deemed obsolete at time of service and those which the time and energy to repair significantly outweighs the cost required to produce or acquire a new component [23]. This capability has become of interest to the mold and die and aerospace industries, wherein significant cost savings could be achieved through integrated repair methods. Components which were once either replaced when worn or repaired by painstaking manual processes can be repaired in a single automated hybrid manufacturing system [24, 25]. Though these machines have been a topic for research for

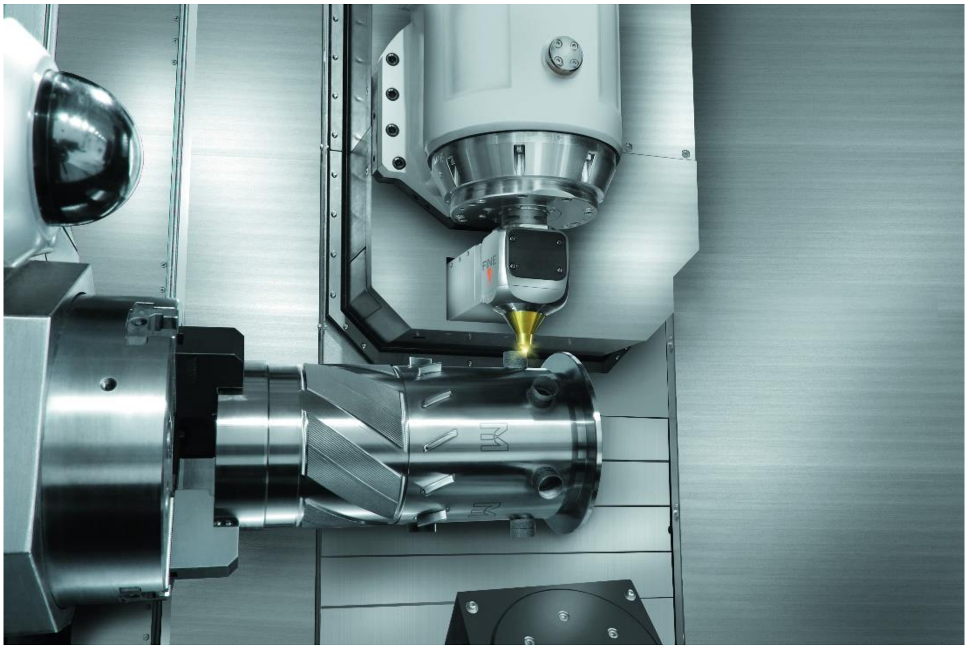

Figure 1: Material deposition in a commercial hybrid manufacturing system: Mazak INTEGREX i-400AM (Advanced Manufacturing)

quite some time [26, 27], only recently have machine tool manufacturers introduced commercially-available hybrid systems, thus underscoring the need for advanced process planning methods and computer-aided manufacturing (CAM) tools to support their implementation.

Currently, several machine tool manufacturers offer machines which combine additive and subtractive processes. The Matsuura LUMEX series combines powder bed laser sintering processes with precision 3 axis CNC machining [28]. Switching between sintering and machining processes between layers allows for the finishing of deep grooves in components which otherwise would require secondary processing. However, this powder base process would not be capable performing component repair. The Hermle MPA C-40 utilizes a thermal spray technique to deposit powder onto a substrate. The particles are accelerated by high pressure gas and undergo high plastic deformation upon impact with the substrate, causing them to bond to the surface. This method also allows for the manufacture of mixed material components, such as copper on steel [29].

The most notable commercial hybrid manufacturing systems, however, feature directed energy deposition systems. Examples of this machines include the DMG Lasertec 65 hybrid and the Mazak AM series which include both table-table five axis and mill-turn machine configurations [20, 30]. Both of these machines are multi-axis configurations, featuring two rotary axes in addition to the standard 3 linear axes. This permits complete access to the component at any point during the manufacturing process, allowing deposition or machining to occur at orientations other than normal to the X-Y plane.

To complement this capability for multi-axis repair, conventional hybrid machines can also be equipped with high accuracy strain gauge style inspection probes. These devices allow for the implementation of measurement-based routines such as automatic part set-up and alignment, machine tool qualification, and mid cycle part inspection and

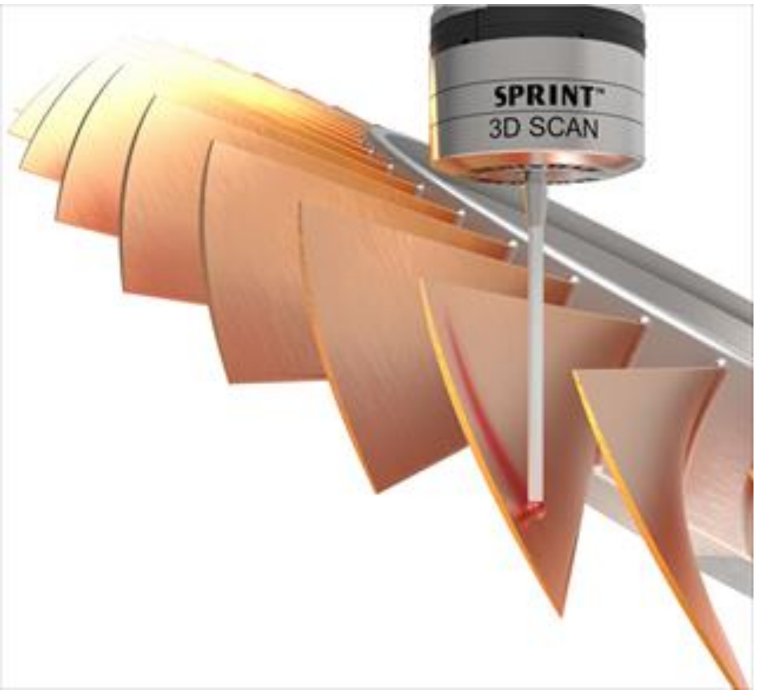

Figure 2: Scanning on-machine inspection probe (Renishaw)

qualification. With repeatability errors and errors due to lobing effects as low as 0.25 μm and 1.0 μm, these devices are capable of performing final part inspection and qualification of components using discrete probing strategies. New scanning style inspection probes allow for rapid qualification of components by remaining in contact with the surface while translating and capturing data, achieving speeds as high as the rapid speed of the machine tool [31]. The data gathered from these on machine inspection systems can then be used to influence pre-programmed routines stored on the machine tool controller or can be exported to a networked pc for further processing.

2.2 Data registration

The purpose of data registration is to transform two or more data sets in order to align corresponding features or regions within the same coordinate system. These data sets pertain to a particular object captured from different viewpoints, produced using different methods, or which relate to objects moving in time. Two methods considered here are rigid and non-rigid registration methods. Rigid registration assumes that the data sets can be related to each other by a single rigid transformation, or the combination of rotation and translation by altering only six degrees of freedom. These algorithms are used in a variety of different fields including 3D mapping, robotic vision systems, and 3D object scanning. Non-rigid registration allows for deformation of data sets in addition to rotation and translation, allowing them to cope with soft bodies or deformation over time [32]. Overall, the objective of these registration algorithms is to minimize the root mean squared (RMS) error between the data sets. However, the number of parameters which must be optimized, e.g., the distances between individual data points, often greatly out numbers the governing equations. This creates a non-linear least-squares optimization problem, which often cannot be solved analytically. However, methods have been developed to approach this problem, several of which will be described.

Feature based registration methods are commonly used in association with a priori knowledge of the geometry, such as common geometric elements. Assuming a small uncertainty in data acquisition and distinguishable features, these methods can provide accurate and consistent alignments. One of the simplest examples of feature-based registration is 3-2-1 alignment. Commonly used for datum alignment, this method sequentially constrains the six degrees of freedom of an object. This method can be executed simply by utilizing the minimum number of points for each feature (i.e. a plane, a line, and a point), or additional data points can be averaged to reduce the uncertainty in the component features. Geometric features can also be fit to a data set (i.e. lines, planes, arcs) using regression methods, which can then be matched to corresponding features on other data sets by the prioritization of fitment based on datum hierarchy. The use of markers is another common technique for the registration of multiple data sets captured of a single object scene from multiple angles. These markers establish a consistent coordinate system which all data sets reference [33].

If corresponding features or points occur between the two data sets, singular value decomposition (SVD) can be used to minimize the distances between correspondents [34]. First the centroids of each data set, p and p', are calculated, and both data sets are centered. Distances from the centroid for each data set are calculated and used to calculate the cross-correlation matrix H, as in Eqs. (1)-(3)

$$q_i = p_i - p \tag{1}$$

$$q_i' = p_i' - p' \tag{2}$$

$$H = \sum_{i=1}^{N} q_i (q_i')^T \tag{3}$$

Using the single value decomposition, H can then be calculated. V is defined as the eigenvectors of $H^T H$, U is the eigenvectors of HH^T, and the diagonal elements of S are the square roots of the eigenvalues calculated in the previous steps. The SDV of H is shown in Eq. (4), and the optimum rotation matrix R is calculated in Eq. (5):

$$H = USV^t \tag{4}$$

$$R = VU^t \tag{5}$$

This rotation matrix and the previous translations required to centralize the data can then be used to align the data. However, this method can be affected greatly by measurement noise or uneven data distribution across samples [35].

Principal component analysis (PCA) is a commonly used technique to reduce the dimensionality in a data set by transforming the data set into uncorrelated principle components [36, 37]. In 3D registration of geometric data, this method can be used to align data sets based on their variance. If the datasets represent objects of similar shape and point distribution, the orientation of variance between the two data sets should also correspond. The major directions of variance in a data set can be determined by computing the eigenvectors of the 3 x 3 covariance matrix calculated from 3D point data [38]. The eigen values obtained from this analysis correspond to the magnitude of variance along their corresponding eigenvector. By aligning eigenvector pairs of two data sets based on eigen value magnitude, the two datasets can be aligned. While this PCA does provide a method for aligning 3D geometry, the minimization method used does not take into account the Euclidean distances between the data sets, only variance. Thus, this method produces undesirable results when faced with differences in point distribution and outliers between the two data sets.

However, these methods do not seek to minimize the overall error between the data sets via direction interpretation of the Euclidean error between the two data sets. For this reason, it is common to conduct registration in a multi-step process. Initial alignment is completed using a non-iterative method, which can quickly be done by assigning similar features or attributes. Then, final registration is completed using an iterative optimization to minimize error in alignment [39].

The most commonly used iterative method for registration is the iterative closest point (ICP) method [40, 41]. This method requires no correspondence between data sets and iteratively disregards outliers. First, this method performs a nearest neighbor search to determine the closest point p'_j to a point p_i in the fixed point cloud, as in Eq. (6):

$$p_j = \arg_i min\left[\|p_i - p'_j\|\right] \tag{6}$$

The rotation and translation, R and T, which minimizes the total RMS error between the two datasets, is then calculated similarly to SDV. This optimum transformation is shown in Eq. (7), where N is the number of points in the transformed point cloud:

$$R, T = \arg_{\mathrm{R,T}} min \sum_{i=1}^{N} \|(Rp_i + T) - p'_i\| \tag{7}$$

These steps are then executed iteratively until the algorithm reaches some termination requirements (i.e. number of iteration, total error, error decrement). However, if the initial alignment of data sets contains gross errors, the algorithm is prone to converge to local minimum error. This reinforces the need for multiple steps in the registration process. A quality initial alignment will allow for faster convergence of an iterative registration algorithm, such as ICP. While this algorithm has been shown to accurately perform registration, the computing cost is relatively high due to iteration in the nearest neighbor search and registration, which compounds for increases in data size. Methods have been developed to accelerate this nearest neighbor search. The integration of k-dimensional binary search trees (k-D trees) sections data into regions and steps through these sequentially rather than iterating through each point in the data set [42]. These iterative methods can also be used for the registration of multiple data sets. In the stitching of individual scans to form one large data set, individual scans can be iteratively aligned to form a complete data set [43]. Pairwise registrations can also be performed on data subsets, which can then be aligned globally with corresponding elements in the subsets [44].

Since these algorithms iterate through incremental rotations and translations, extrapolations can be performed if trends are realized in error throughout the registration process. As the needs of data registration have grown, many adaptations of the ICP algorithm have been developed for varying situations. Hierarchal ICP algorithms have been developed for the registration of triangle meshes which localizes the search regions in the nearest neighbor search to similar triangle regions [45]. For the registration of surfaces, modified ICP algorithms have been developed which manipulates control points and performs interpolation between surfaces and defining geometry [46].

Iterative registration techniques have also been used to perform non-rigid registration of components. These processes not only have to account for all challenges associated in rigid registration, but also must account for any deformation between the data sets. These problems are often faced in the registration of medical data, where deformations can occur from changes in soft tissue and features which may change over time [47]. A major challenge for these methods is to determine data correspondence. To capture correspondences, template surfaces can be registered to each data set, where each vertex's movement can be captured by a rotation and translation. The transformations applied to the template surfaces can then be compared to register the data sets [48]. Localized ICP operations can also be performed in areas of higher deviation in order to preserve fine details in data sets [49]. However, these methods are often computationally expensive, as they require the minimization of many simultaneous cost functions.

2.3 Reverse modeling of aerospace components for repair

Repairs on jet engine components are crucial in the maintenance of the nation's commercial airlines. With component costs reaching as high as $500,000, scheduled inspection and repair is critical to maintain the economic viability of air travel [50, 51]. These repair processes include, but are not limited to, the removal and re-deposition of worn coatings, the repair of worn surfaces on stationary components, and re-machining of bushing surfaces. One of the most common repair practices is the re-manufacture of compressor blade tips. In normal operation, these blades experience wear at their tips, thus increasing the clearance between the compressor and housing, which acts to decrease the efficiency of the engine [52]. These components may also experience damage from foreign object debris (FOD), which can bend and distort their geometry.

These airfoil components are often repaired using a complex restoration process, a simplified version of which is shown in Figure 3. First, the worn area is removed from the blade tip by machining. Material is then deposited on the blade using an additive process (e.g., directed energy deposition, welding) as in Figure 3(b). Finally, the surface is machined and blended to final form in Figure 3(c). Final machining and blending is complicated by the fact that, during use, airfoil blades in particular may experience varying

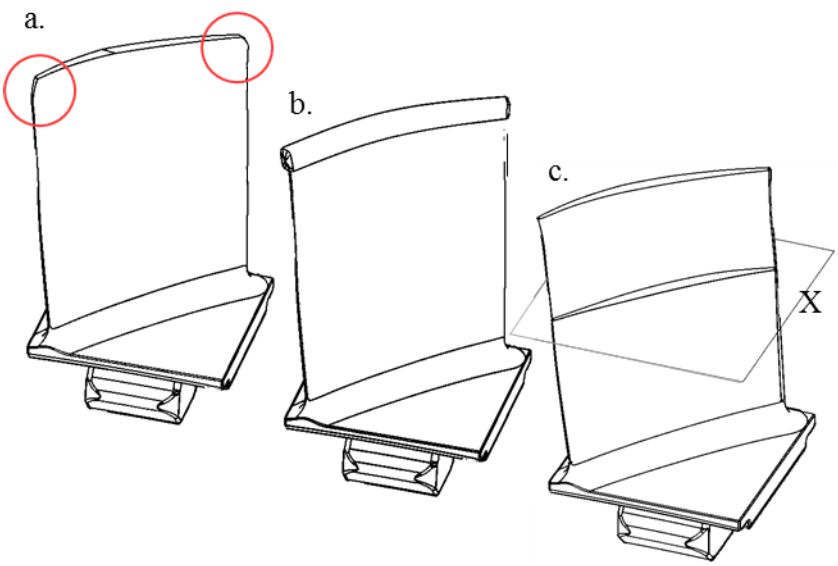

Figure 3: Image of compressor blade through various stages of repair process. Starting as a worn in use part (a.), adding material to build up cut back material (b.), fully repaired blade after machining.

degrees of distortion. The potential variations in geometry must be considered in the final blend repair, rendering use of static toolpaths insufficient. To account for these changes, excess material is added during deposition and a safety margin is designed to be left after machining so to minimize the chances of gouging the parent material. In this case, final blending of this remaining material into the parent blade material is often done using a manual blending method to ensure a smooth transition between the repaired region and the original blade.

This manual hand blending process is not only time consuming and costly, but also leads to an inconsistent process and erratic final product quality due to variations in the human interaction required to complete this difficult task. This blending process has been automated in some instances by using robotic grinding/polishing cells [53]. However, if the final finishing process could be completed in the machine tool, significant process savings could be realized. Bremmer described then need for the linking of 4 critical steps in the repair process: inspection, weld preparation, welding, and re-profiling [54]. This was further developed into the concept of adaptive machining processes, defined for components which have individual shapes which cannot be manufactured with fixed programs [55]. In order to accomplish these adaptive repair techniques, a unique set of tool paths for both the additive and subtractive phases must be generated for each unique starting geometry. This requires the model these tool paths are derived from to adapt as well, including accurate reconstruction of the remaining parent material and adaptation of the nominal tip geometry which maintains continuity with the parent surface.

Qi et al. described an adaptive additive repair method for compressor blades [56, 57]. This method showed promising results in designing adaptive additive tool paths for compressor blade repair. However, this method adapted only to the region which needed repair and not to the overall geometry of the parent component. Zheng et al. examined reverse engineering of worn areas on aerospace components for additive repair [58]. This method reconstructs broken or worn areas on an actual component by comparing the nominal CAD geometry to a point cloud scan of the part. While this method proved successful in the reconstruction of areas which deviated from the nominal model, this method did not take into account distortions that may occur in the actual blade. Furthermore, no constraints are put in place to ensure surface continuity if the component differs from the nominal model.

Yilmaz et al. demonstrated another method for compressor blade repair utilizing a full reconstruction of the actual blade using structured light scanning [59]. This method showed promise in reconstruction of the final model, as well as accurate results in machining trials. However, multiple scans are required to capture the entire geometry, which must then be registered and combined into a smooth mesh: a process which is reported to take 5 minutes due to the full scan of the blade required to construct the actual geometry.

Yun et al. presented a method for the modelling of compressor blade geometry based on original design intent [60]. This method utilized the adaptation of a profile’s mean camber line to conform to known design requirements to repair the leading and trailing edges of an airfoil. Data captured on the pressure surfaces of the blade is used to inform geometry modifications in the leading and trailing edges. However, no parametrization is used to extend this captured geometry vertically for tip repair. Dong et al. also present a parameterized method utilizing the profile’s mean line [61]. Other presented blade reconstruction methods show promise in reverse engineering the blade geometry, but do not attempt reconstruct the geometry needed to be created in a tip repair process[62-64].

Bagci demonstrated a case study for the reverse engineering and re-manufacture of broken components, and presented a case study for the remodelling of a damaged turbine blade [65]. This method utilized the inspection of several cross sections by CMM. Closed splines were then form from cross sections with data that was deemed to be undamaged. These curves were then used to form surfaces over the geometry. This method however, does not use any prior knowledge to create the final lofted profile, and is created using data from the previous cross sections, which could cause an undesirable geometry in the final profile.

Several of the previously described reverse engineering methods are used for the repair of aero-engine components, however few are applicable to both the additive and subtractive phases of the repair process. Yilmaz et al. state that their model adaptation process could be applied in the additive phase, however this is not shown directly in the literature [66]. Other works have investigated the use of integrated hybrid systems which are capable of adapting on a component by component basis, however little has been stated on how to adapt the tool paths used in the repair [24, 67]. Moreover, little work has been done to fully characterize the gains (e.g., time and material savings) that could realize by implementing a completely adaptive repair process encompassing both additive and subtractive phases of repair.

CHAPTER 3. METHODOLOGY

The adaptive repair strategy is designed for implementation within the framework of an integrated additive/subtractive hybrid manufacturing machine, wherein digitization of part geometry can be accomplished utilizing common on-machine inspection (e.g., strain-gauge style inspection probes). Using this method of data capture, 2D profiles of received part geometries can be digitized, an example of which is shown in Figure 5 for the case example of the present study – a typical compressor airfoil part. With these profiles, nominal CAD data of the component can then be manipulated to match an individual

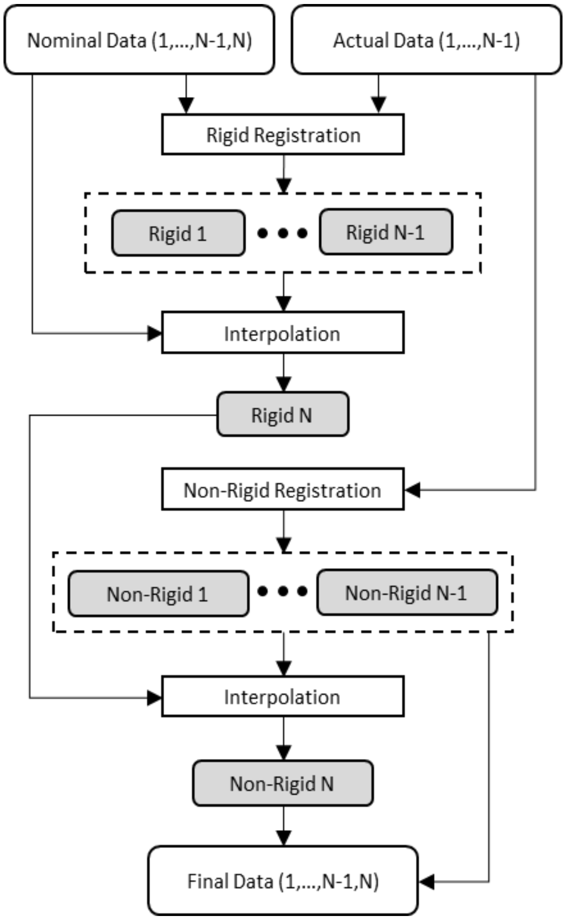

Figure 4: Process for unknown surface modeling

component to be repaired. This transformation method is performed in multiple steps; geometry construction, rigid profile registration, mean line deformation, and profile creation. In geometry construction, individual points probed on 2D cross sections of the component are used to create a mean line and thickness distribution for the profile. In the rigid profile registration, individual cross sections are aligned using an iterative algorithm to minimize the RMS error between them. Mean line deformation deforms the profiles of the nominal CAD data to match that of the measured part geometry. The part geometry within the repair region, in this case the airfoil tip, is then manipulated via interpolation of the previous transformations to alter the final profile of the nominal model. These final profiles can then be used to create a final solid model of the actual part to be repaired. Figure 4 shows the overall adaptive repair sequence resulting from implementation of this algorithm.

3.1 Geometry construction

The actual geometry can be captured by probing K cross sections of the actual component, where K > 2, at predetermined heights along the stacking axis of the profiles and outside of the repair region. The mean line of an individual profile, shown in the cross section of Figure 5, is defined as a continuous curve which lies equidistant to either side of

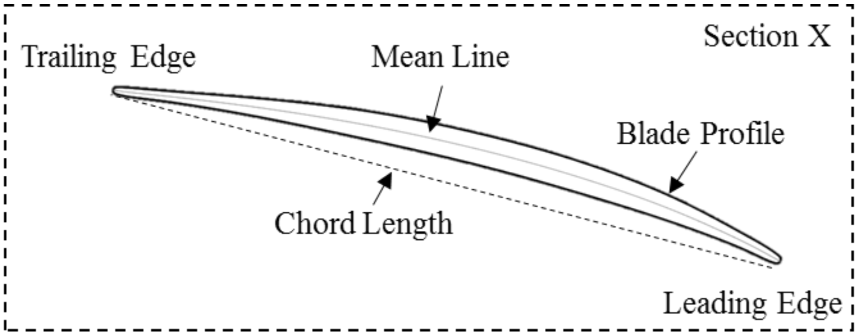

Figure 5: A representative cross section of a compressor blade

the exterior surfaces of the component. The thickness is defined as the perpendicular distance from this mean line to the edge of the blade profile. The mean line can be constructed by analyzing the center points of the minimum inscribed circles fit within the profile.

Once the 2D profile points are imported, defined as a matrix of m 3D points at a height z coordinates $\bar{P}_z = [P_0 \dots P_m]$, the camber line direction is first calculated by searching the data to find the two points P_p and P_q separated by the maximum distance l, as in Eq. (8) and Eq. (9):

$$l(P_a, P_b) = \sqrt{\left(P_{a_{\bar{i}}} - P_{b_{\bar{i}}}\right)^2 + \left(P_{a_{\bar{j}}} - P_{b_{\bar{j}}}\right)^2} \tag{8}$$

$$argmax_{p,q}\, l\left(P_p, P_q\right) := \left\{P_a, P_b \middle| \forall P_p, P_q : l(P_a, P_b) \leq l(P_p, P_q)\right\} \tag{9}$$

The points with the largest distance, P_p and P_q, are then used to form the camber line vector $\bar{c}$. A distribution of points $\overline{D}$ can then be created along the camber line using the camber line vector, the starting point on the camber line, and distribution vector $\overline{d}$, which is represented as an nx1 vector of percentages along the camber line vector, as in Eq. (10):

$$\overline{D} = P_p + \bar{c} * \overline{d} \tag{10}$$

Cubic spline interpolation is performed on the imported probe points to create an equation for the profile curve. Seed points can then be created on the profile by transferring the point distribution $\overline{D}$ onto the curve. These points $\overline{S}$ are then translated inside the curve a predetermined distance *r* along the direction normal to the curve $\overline{n}$ at the points each point in $\overline{S}$. The normal vectors are calculated by evaluating the derivative of the profile $f(t)'$ at each point $\overline{S}$. This radius *r* is used to create circles within the profile defined by Eq. (11) and Eq. (12):

$$Q_x = [s + r\overline{n}] + rcos(\emptyset) \tag{11}$$

$$Q_y = [s + r\overline{n}] + rsin(\emptyset) \tag{12}$$

The radius *r* of these profile circles is then increased gradually until they contact the opposite side of the closed profile curve, forming a sequence of inscribed circles within the profile. The center points of these circles then lie equidistant, separated by *r*, from both sides of the profile. The mean line ML_z of the profile can be constructed by performing spline interpolation on these center points. This mean line is constructed using control point vector $\overline{Cp_z} = [CP_0 \dots CP_n]$, a knot vector $\bar{t}_z = [t_0 \dots t_{n+4}]$, and the b-spline basis functions $N_z = [N_{0,3}(t_z) \dots N_{n,3}(t_z)]$, as in Eq. (13):

$$ML_z(t_z) = \sum_{i=0}^{n} \overline{Cp_{z,\iota}} N_{i,3}(t_z) \tag{13}$$

An example of a calculated mean line is shown in Figure 6. The initial profile can be seen shown in blue, with the calculated camber line vector $\overline{c}$ shown in red. The

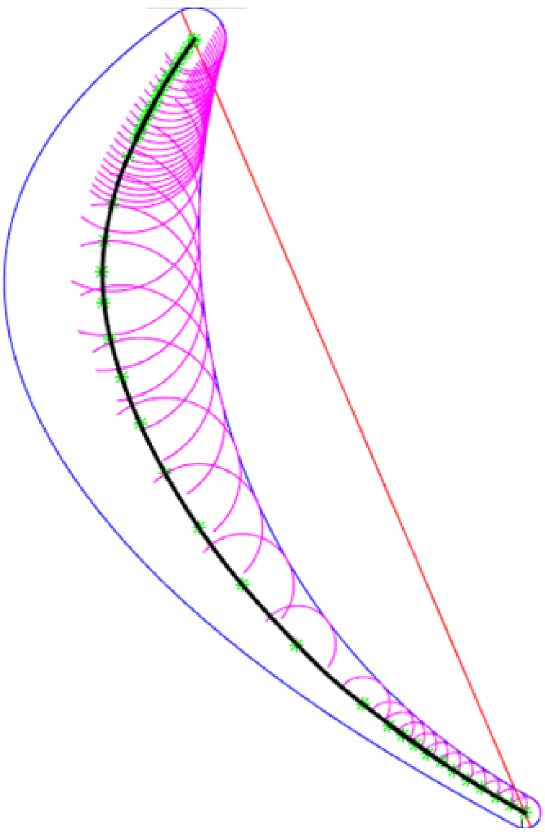

Figure 6: Calculation of a cross section mean line using interpolation of minimum inscribed circles

calculated circles are shown here in purple, with the interpolated mean line ML_z shown in black.

The thickness distribution about the mean line Td_z of this profile can now be calculated. The radii of the inscribed circles can be used to form a function of the knot vector t_z, as in Eq. (14)

$$Td_z = f(t_z) \tag{14}$$

The nominal geometry can then be input as well by evaluating the model using *K*+1 profiles. *K* of these profiles are evaluated on the nominal model at the same heights as on the actual component. To complete the nominal geometry, the K^{th+1} profile is evaluated at the tip of the nominal model. The input nominal data is input similar to the actual where *n* denotes the nominal model as $Pn_z,\ MLn_z(t_z),\ Tdn_z(t_z),$.

3.2 Rigid profile registration

Alignment of the nominal CAD geometry and the actual geometry is performed using a rigid registration algorithm that translates and rotates each of the nominal profiles relative to the respective actual profiles. Due to distortion or deformation that may be present in the actual component, each individual profile must be registered. Each nominal profile Pn_z is registered with its counterpart actual profile P_z. Doing so accounts for distortions which change the location of a profile relative to the adjacent profile, i.e. P_i relative to P_{i+1}. This rigid registration is capable of aligning the two data sets in 3D space, as well as capturing any changes between profiles such as blade twist. Twist (θ), shown in Figure 7, is defined here is defined as planar rotation of a profile about the radial axis of the blade. This rigid registration is completed using an iterative closest point (ICP)

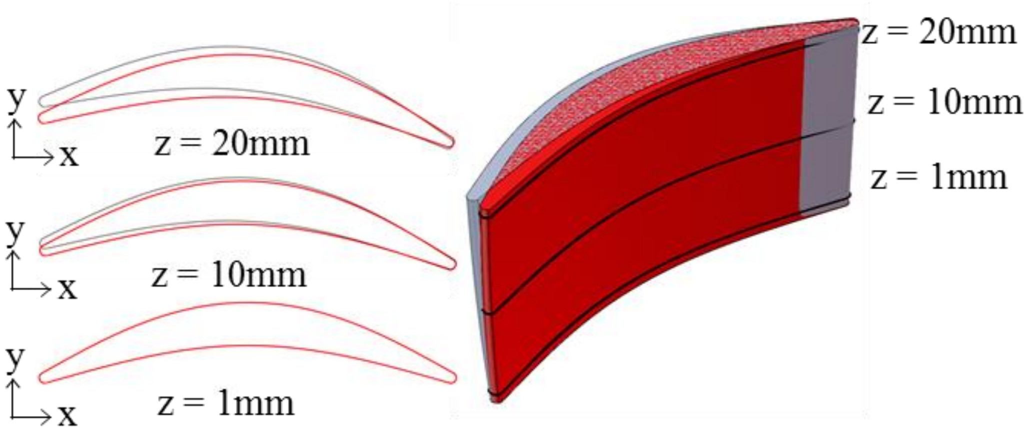

Figure 7: Example of an actual part and its nominal CAD model, shown in red and grey respectively, with blade twist (θ

algorithm, which minimizes the least squared error between the two point sets. The ICP algorithm is iterated until the decrement in error between successive iterations is less than 0.1%. The final 3 x 3 rotation matrix R and 3 x 1 translation T are then stored. This operation is performed for K profiles on the actual geometry, yielding $R_z = [R_1 \dots R_K]$, and $T_z = [T_1 \dots T_K]$.

The $K^{\text{th}+1}$ profile of the nominal geometry must be transformed as well. However, no information is available regarding the $K^{\text{th}+1}$ profile of the actual component, so an informed alignment must be calculated using the previous K profile transformations. In the case of K = 2, a linear interpolation can be made based on the data. Higher order interpolations are possible for greater values of K, which could lead to greater accuracy in the construction of the final model. Using only two sections, R_{K+1} and T_{K+1} can found by linear interpolation using $[R_1, R_2]$ and $[T_1, T_2]$. To calculate R_{K+1}, R_1 and R_2 must be split into their respective Euler rotation components: θ_x, θ_y, and θ_z. These individual components can be calculated using a method similar to that detailed in reference [68].

R can be defined as the product of three individual Euler transformations $R_x(\theta_x)$, $R_y(\theta_y)$, and $R_z(\theta_z)$, as in Eqs. (15)-(18):

$$R_x(\theta_x) = \begin{bmatrix} 1 & 0 & 0 \\ 0 & \cos(\theta_x) & -\sin(\theta_x) \\ 0 & \sin(\theta_x) & \cos(\theta_x) \end{bmatrix} \tag{15}$$

$$R_y(\theta_y) = \begin{bmatrix} \cos(\theta_y) & 0 & \sin(\theta_y) \\ 0 & 1 & 0 \\ -\sin(\theta_y) & 0 & \cos(\theta_y) \end{bmatrix} \tag{16}$$

$$R_z(\theta_z) = \begin{bmatrix} \cos(\theta_z) & -\sin(\theta_z) & 0 \\ \sin(\theta_z) & \cos(\theta_z) & 0 \\ 0 & 0 & 1 \end{bmatrix} \tag{17}$$

$$\begin{aligned} R = {} & R_x(\theta_x)\, R_y(\theta_y) R_z(\theta_z) \\ = {} & \begin{bmatrix} \cos(\theta_y)\cos(\theta_z) & \sin(\theta_x)\sin(\theta_y)\cos(\theta_z) - \cos(\theta_x)\sin(\theta_z) & \cos(\theta_x)\sin(\theta_y)\cos(\theta_z) + \sin(\theta_x)\sin(\theta_z) \\ \sin(\theta_y)\cos(\theta_z) & \sin(\theta_x)\sin(\theta_y)\sin(\theta_z) + \cos(\theta_x)\cos(\theta_z) & \cos(\theta_x)\sin(\theta_y)\sin(\theta_z) - \sin(\theta_x)\cos(\theta_z) \\ -\sin(\theta_y) & \sin(\theta_x)\cos(\theta_y) & \cos(\theta_x)\cos(\theta_y) \end{bmatrix} \end{aligned} \tag{18}$$

The individual angles can then be calculated as in Eqs. (19)-(212121):

$$\theta_y = -asin(R_{3,1}) \tag{19}$$

$$\theta_x = atan2\left(\frac{R_{3,2}}{\cos(\theta_y)}, \frac{R_{3,3}}{\cos(\theta_y)}\right) \tag{20}$$

$$\theta_z = atan2\left(\frac{R_{2,1}}{\cos(\theta_y)}, \frac{R_{1,1}}{\cos(\theta_y)}\right) \tag{21}$$

However, this method yields two possible solutions for the rotation. The incorrect solution can be ruled out by transforming Pn_z by the two sets of calculated components and comparing the RMS error. The linear interpolation for the component rotations can then be completed according to Eqs. (22)-(24):

$$\theta_{x,3} = \frac{\theta_{x,2} - \theta_{x,1}}{z_2 - z_1} * (z_3 - z_2) + \theta_{x,2} \tag{22}$$

$$\theta_{y,3} = \frac{\theta_{y,2} - \theta_{y,1}}{z_2 - z_1} * (z_3 - z_2) + \theta_{y,2} \tag{23}$$

$$\theta_{z,3} = \frac{\theta_{z,2} - \theta_{z,1}}{z_2 - z_1} * (z_3 - z_2) + \theta_{z,2} \tag{24}$$

The rotation matrix for the K^{th+1} profile is calculated by combining the individual X, Y, and Z rotations, regardless of the order of interpolation applied, as in Eq. (25):

$$R_{K+1} = R_z(\theta_{z,K+1})R_y(\theta_{y,K+1})R_x(\theta_{x,K+1}) \tag{25}$$

The translation T_{K+1} is calculated similarly to R_{K+1}, based on the order of interpolation. The calculated transformations can then be applied to all K+1 profiles and profile mean lines by translating the profile points, Pn_z, and spline control points, Cpn_z. The transformed profiles PT_z, transformed control points CpT_z, and transformed mean lines MLT_z can be found according to Eqs. (26)-(28):

$$PT_z = R_z Pn_z + T_z \tag{26}$$

$$CpT_z = R_z Cpn_z + T_z \tag{27}$$

$$MLT_z(t_z) = \sum_{i=0}^{n} CpT_{z,i} N_{i,3}(t_z) \tag{28}$$

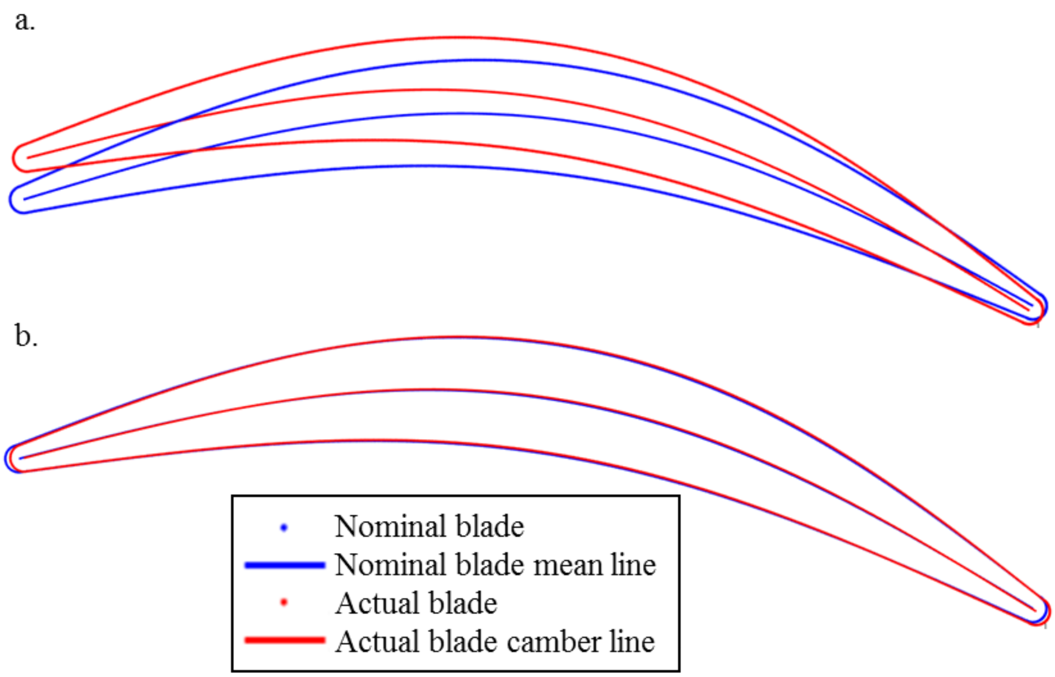

Figure 8: Comparison of (a.) before and (b.) after rigid registration

Figure 8 shows an example of the transformation of one profile using the ICP method described in this section. The nominal blade profile and mean line have been rotated and translated to minimize the RMS error between the two data sets. However, errors do still appear. While the RMS error between these two data sets has been minimized, the deformations which occur within the individual profile of the actual blade cannon be resolved using this method alone.

3.3 **Mean line registration**

Deviations in mean lines, and therefore deviations in the profile geometry, are addressed in this algorithm by comparison of the mean lines between the actual and nominal geometry, ML_z and MLT_z. An example of this is a compression of the blade within the profile plane, thus resulting in a change in chord length (ΔC). This type of deformation is shown in Figure 9. By using this mean line registration, the algorithm is capable of capturing variation which may occur in the form of an individual profile. The form of these mean lines can be compared by examining the spline control points. The deviations between corresponding control points can be defined as D_z, and are evaluated for K profiles, as in Eq. (29):

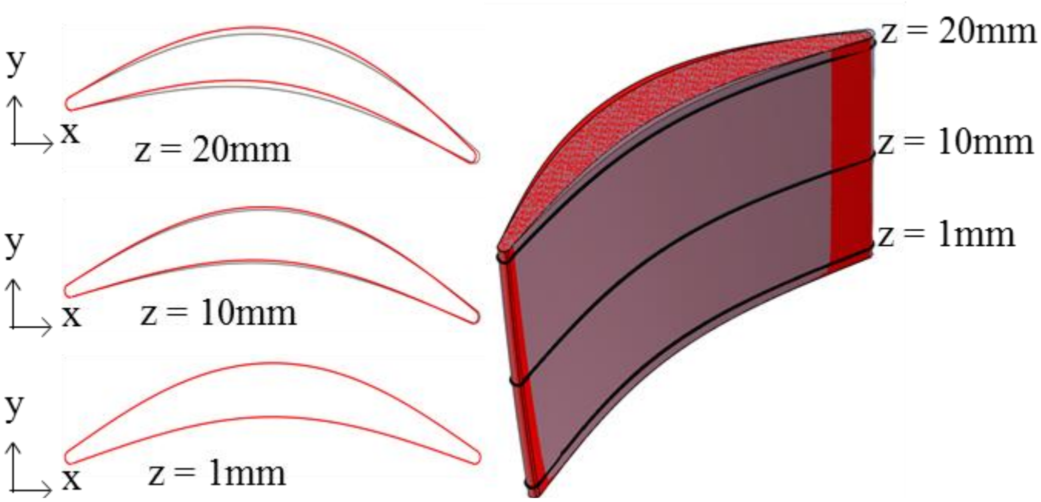

Figure 9: An example of chord compression (*ΔC*) on an actual blade (red) and it's nominal model (grey)

$$D_z = Cp_z - CpT_z \tag{29}$$

Similar to the rigid registration, the $K^{\text{th+1}}$ mean line is also manipulated via an interpolation function. If K=2, then D_{K+1} is calculated using a linear interpolation, as in Eq. (30):

$$D_{K+1} = \frac{D_K - D_{K-1}}{z_K - z_{K-1}} * (z_{K+1} - z_K) + D_K \tag{30}$$

For this case of $K = 2$, this is done using a linear interpolation on a control point by control point basis. The adapted nominal control points for each spline can then be calculated as in Eq. (31):

$$Cpf_z = CpT_z + D_z \tag{31}$$

Then, the final mean lines MLF_z can be calculated as in Eq. (32):

$$MLF_z(t_z) = \sum_{i=0}^{n} Cpf_{z,i} N_{i,3}(t_z) \tag{32}$$

These final mean lines can then be used to form the final profiles.

An example of this mean line manipulation can be seen in Figure 10, which shows a correction of mean line for a particular profile. In Figure 10(a), the deviation between the nominal and actual profile can be seen, as well as deviation in the control points and polygon which define the spline. In Figure 10(b), this deviation has been corrected. The control polygon and points are aligned, and the mean lines appear unified with minimal deviation.

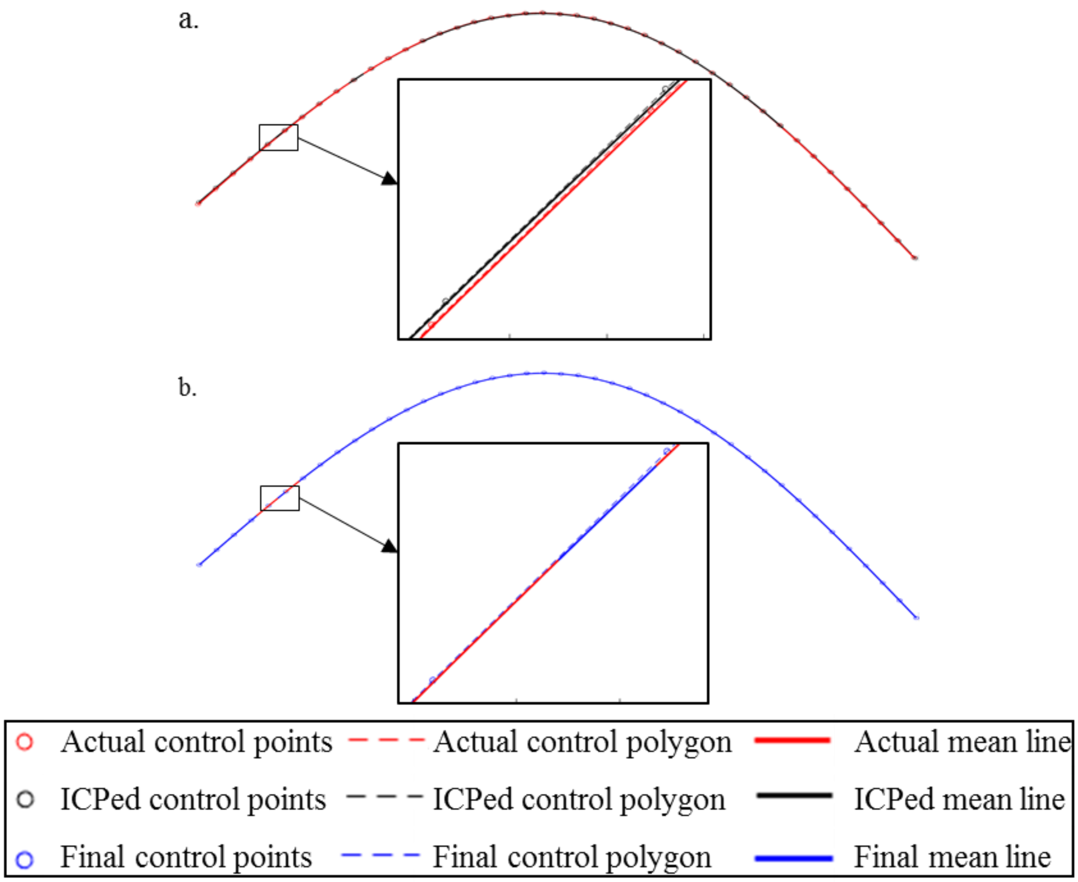

Figure 10: Correction of deviation between actual and nominal mean line. Original mean line shown in (a.) and corrected shown in (b.)

3.4 Profile creation

After the mean lines have been manipulated, the final blade profiles can be generated by assessing the profile thickness distribution along corresponding profile mean lines. First, the mean line derivatives MLF_z' are calculated. Using these derivatives, vectors perpendicular to the curve, defined as $N_z(t)$, can be calculated within the XY plane and normalized. To create the final profile PF_z, the final mean line MLF_z is sampled at the desired density and points are placed on either side of the final mean line at a distance

Td_z along the normal vector N_z. The actual thickness distribution Td_z is used to evaluate the final profiles for the non-repair region, while the nominal thickness distribution is used for evaluating the final profiles for the K^{th+1} profile. The final profiles for each contour (e.g., $z = 1,..,K+1$) are evaluated using general form as in Eq. (33):

$$PF_z = MLF_z(t) \pm Td_z(t)\overline{N_z}(t) \tag{33}$$

However, while this applies for either side of the mean line, the end condition for a particular profile may change. For instance, in the case of a compressor blade the ends of the profile are rounded to create the leading and trailing edge radii. In order to create this geometry, the thickness distribution is created such that the knot vector extremum (i.e. $t = 0,\ t = t_{max}$) are equal to the leading and trailing edge radii respectively. At $t = 0$, an arc is created which spans between the previously created profile points and is centered at $MLF_z(0)$. The starting angle for the span φ_{start} is interpreted by calculating the angle between the positive X axis in the plane and the vector formed by the arc center point and the point on positive side on the final mean line, as in Eq. (34). A similar procedure is done for the end angle φ_{end} by using the point on the negative side of the profile, as in Eq. (35):

$$\varphi_{\mathrm{start}} = \cos^{-1}\left[\frac{\left(\overline{e_1} \cdot \overline{\boldsymbol{N_z}(0)}\right)}{|\overline{e_1}|\left|\overline{\boldsymbol{N_z}(0)}\right|}\right] \tag{34}$$

$$\varphi_{end} = \cos^{-1}\left[\frac{\left(\overline{e_1}\cdot(-\overline{\boldsymbol{N_z}(0)})\right)}{|\overline{e_1}|\left|\overline{-\boldsymbol{N_z}(0)}\right|}\right] \tag{35}$$

The angle span φ is then sampled at a density similar to the profiles. The X and Y coordinates $P_{z,x}(i), P_{z,y}(i)$ for these points are calculated using the angle φ(i), the thickness distribution $Td_z(0)$, and the center point $MLF_z(0)$, as in Eq. (36) and (37).

$$P_{z,x}(i) = Td_z(0)cos\big(\varphi(\mathrm{i})\big) + \ MLF_z(0) \tag{36}$$

$$P_{z,y}(i) = Td_z(0)sin\big(\varphi(\mathrm{i})\big) + \ MLF_z(0) \tag{37}$$

Similarly, the other profile end can be calculated by following the previous steps using $t = t_{max}$. These points can then be appended to previously calculated profile points to form the entire list of profile points. This is then repeated for all *K*+1 sections. A closed curve is then fit to these curve points to form the profiles. The final solid model for the adapted model can then be created by lofting the individual profiles.

3.5 Geometry definition

Several blade geometries were created for the purpose of testing and validating this registration algorithm, which is discussed in chapter 4. This section will detail the creation of these geometries, including the driving equations and parameters used. Each geometry is initially defined by the mean line, which is then translated vertically and rotated about the origin to form multiple cross sections. Once the mean line is established for each section, the profiles can be created using a defined thickness distribution and the method described in the previous section. Deformed blades can be calculated by adapting the nominal mean line equations.

3.5.1 Nominal geometry definition

The nominal geometry was first defined by the mean line of the profile occurring in the X, Y plane at Z = 0. This mean line was defined by Eq. (38), and was bounded:

$$y(x) = .25 \sin\left(\frac{\pi x}{.1875}\right) \quad 0 \leq x \leq 1.875 \tag{38}$$

This curve was then sampled *n* times to create a 3x*n* set of mean line points L_1. After the creation of the mean data set, the origin must be shifted to lie on an appropriate position for the stacking axis. The data set was shifted by -1.675 in X and by -0.0822 in Y to place origin at an appropriate position which lies on the mean line. Two additional profiles were created, allowing the previously described registration algorithm to perform interpolation with $K = 2$. To create these two additional profiles, the mean line data set L_1 was translated in Z and rotated about the stacking axis of the blade, which in this case is defined as the origin of the X, Y plane. The heights for the different profiles and the corresponding rotation at that height were defined as $Z = [0\ .375\ .875]$ and $\psi_z = [0 - 3 - 6]$ respectively. These rotations and translations are then applied, as in Eq. (39):

$$L_Z = R_z(\psi_z)L + \begin{bmatrix} 0 \\ 0 \\ Z \end{bmatrix} \tag{39}$$

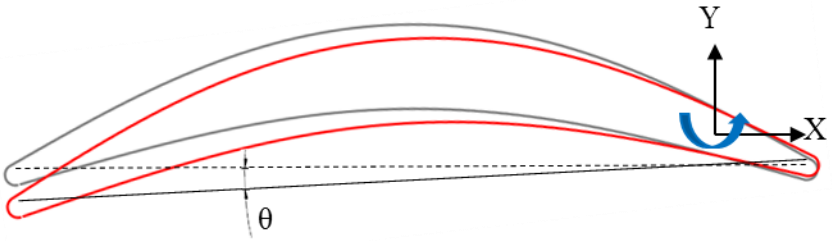

Figure 11: Creation of twist θ for an individual profile with the original shown in grey and Twisted shown in red

With the mean line point sets for the three profiles created, cubic spline interpolation can then be performed to form the cubic spline representation of the mean line, which is used in the registration algorithm. Using the spline equation for the mean line, the profile can then be constructed using the previously described method and a defined thickness distribution. For each profile constructed, the thickness distribution was identical and was defined as in Eq. (40):

$$Td_z(t) = .075\sin\left(\frac{t\pi}{t_{max}}\right) \quad 0 \leq t \leq t_{max} \tag{40}$$

3.5.2 Deformed geometry creation

Deformed geometries created for experimentation were created in a similar matter. The deformation values, θ and ΔC, are first input into the geometry creation. The change in chord length and profile twist for each cross-sectional profile are simply θZ and ΔCZ, as the values are proportional to the increase in Z along the radial direction of the blade. Because of this change in chord length, the values used to define the range used in Eq. (38) must be changed accordingly. Furthermore, the mean line should be required to curve inward or outward in order to maintain a constant arc length to simulate the bowing of the

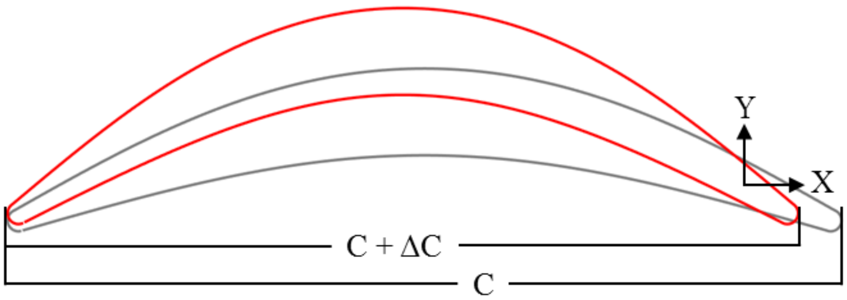

Figure 12: Creation of camber line change for a given profile with the original in grey and compressed shown in red

blade. A constant *m* is inserted in Eq. (38) to accomplish this, which changes for varying levels of deformation, thus, resulting in the definition of the mean line, as in Eq. (41):

$$y(x) = msin\left(\frac{\pi x}{(.1875 + \Delta CZ)}\right) \quad 0 \leq x \leq .1875 + \Delta CZ \tag{41}$$

The value of *m* used in this Eq. (41) varies from profile to profile and from blade to blade based on the deformation used. Since the arc length of the nominal profile, λ, must remain constant the value of *m* which produces this arc length can be calculated by solving for *m* in Eq. (42):

$$\lambda = \int_{0}^{.1875+\Delta C_Z} \sqrt{1 + (y'(x))^2}\, dx \tag{42}$$

Once the full equation for the mean line is calculated, the mean line can be sampled similar to the nominal geometry to create the mean line point set *L*. The pointset is then translated to the appropriate location for the stacking axis. Due to changes in mean line geometry, this position in Y which lies on the mean line will also change. Therefore, this translation is defined as a function of ΔC*Z*. The point set must also be rotated and translated in Z to account for the nominal orientations and locations of the profiles. Twist is then applied to the individual profiles by adding θZ to nominal rotation ψ_z. This final combination of transformations used to define the profiles can be seen in Eq. (43):

$$L_z = R_z(\psi_z + \theta Z\ )L + \begin{bmatrix} -1.675 \\ -msin\left(\frac{\pi 1.675}{(.1875 + \Delta\mathrm{CZ})}\right) \\ Z \end{bmatrix} \tag{43}$$

CHAPTER 4. RESULTS AND DISCUSSION

This chapter summarizes the results of simulations designed to investigate the performance and applicability of the previously described model transformation method. First, the performance of the algorithm is measured by testing the accuracy of a deformed blade compared to the actual geometry. Then, the accuracy of the blend region is assessed to ensure continuity between the machined repair and the parent material in this critical area. Potential process gains are then assessed by examining material efficiency in the additive repair phase of the hybrid repair process. Finally, potential time savings in the subsequent machining process are then examined by performing simulations using adaptive/subtractive toolpaths.

4.1 Evaluation of algorithm performance

For the purpose of model validation, a representative nominal model geometry was created from a pre-defined mean line and thickness distribution at three cross sections. These three profiles were then lofted to create a final solid model. Simulation of deformations to the nominal model were made by introducing both twist and chord length changes to the nominal model, both of which are expected distortion conditions in the repair of compressor blades. Twist in the blade was created by rotating the blade profiles about the blade radial axis, while chord manipulations were created by modifying the profile mean line for the individual sections. Chord length changes were made by translating the tips of the blade at controlled distances, while the profile mean line was bowed or stretched in order to preserve the arc length of the curve. Twist applied to the

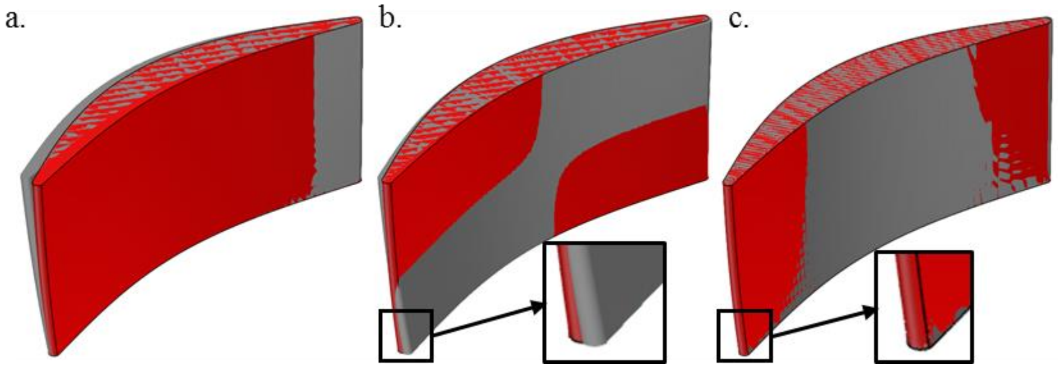

Figure 13: Comparison of rigid registration methods on final blade geometry with actual blade geometry (red) and nominal geometry (grey): Initial alignment (a.), model ICP (b.), profile ICP (c.)

blade θ varied between ±0.118°/mm in increments of 0.0394°/mm and chord length changes ΔC varied between ±2.28e-3 mm/mm in increments of 0.0011428 mm/mm.

First, an actual blade with deformation parameters θ = 0.118°/mm, ΔC = -2.28e-3 mm/mm was generated to examine the effect of rigid registration of individual profiles vs the rigid registration of the model as a whole. This actual blade and a nominal model were first rigidly aligned using the same ICP algorithm. In a different case, the actual and nominal models were input into the rigid registration portion of the previously described algorithm. Figure 13(a) shows the initial alignment of these two models; the actual and nominal models shown in red and grey respectively. Figure 13(b) shows the two models after rigid registration of the entire nominal model to the actual data. Large deviations can be seen between these two models, especially at the lowest profile. This is expected, as the rigid registration is unable to detect regional deviations in the alignment. Figure 13(c) shows the results of rigid registration of the individual profiles. This method shows significant improvement over the overall rigid alignment of the models.

4.1.1 Evaluation of algorithm against full models

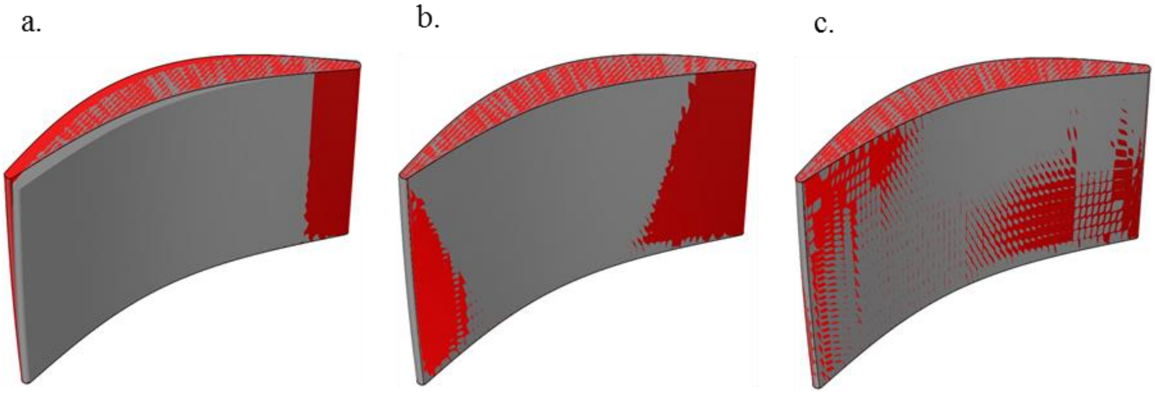

Figure 14: Evolution of nominal geometry (grey) throughout the registration process in comparison with actual geometry (red); (a) nominal geometry, (b) rigid registration, (c) profile mean line transformation

An actual (deformed) blade with deformation parameters θ = -0.118°/mm, ΔC = -2.28e-3 mm/mm was generated to first test the algorithm. Figure 14(a) shows models for both the actual blade (in red) and nominal model (in grey). This actual geometry was input into the previously described algorithm with K=2 with a linear interpolation completed to register the final profile. The profiles are first rigidly transformed and registered using the ICP algorithm, which acts to minimize the overall distance between a nominal profile and its corresponding actual profile. The transformation of the final profile within the repair region is then interpolated based on the transformed profiles which are derived from the actual input geometry. Figure 14(b) shows the two models after rigid transformation. While the profiles have been roughly aligned in space to one another, some deviation remains between the two profiles, mainly in the center of the blade where chord compression has bowed the profile mean line. The deviation from the surface shown in Figure 14(b) can be seen in Figure 15. Despite the largest region of deformation occurring on the concave pressure surface of the blade, the largest deviations occur at the tips of the leading and trailing edges. This is where the largest deviation is expected to be, as the deformation of

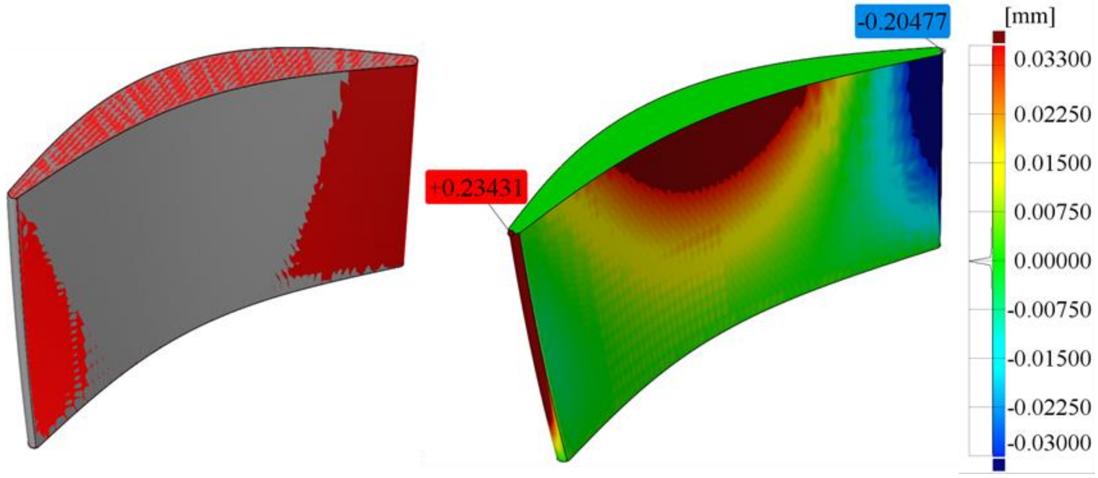

Figure 15: Surface comparison: (a) ICP transformed nominal in grey with actual data shown in red (b) deviation map

this profile is a product of interpolation function used. In this case, the maximum and minimum deviations respectively are +0.234 mm and -0.204 mm. In this case, positive deviations describe regions in which the deformed nominal lies outside, or is larger than, the intended actual geometry, while negative values indicate regions which lie within, or are smaller than, the intended actual blade geometry. Figure 14 (c) shows the model after final manipulation of the mean line, which should match the nominal mean lines to the corresponding mean line on the actual model. The remaining deviations associated with this final deformation are presented in Figure 16. While the maximum and minimum deviations, +0.0123 mm and -0.0092 mm respectively, still occur along the leading and trailing edges of the blade, the magnitude has significantly decreased. A summary of the deviation report for each step of the algorithm is reported in Table 1. The mean deviation after final registration has decreased to 0.3 μm, with the standard deviation of the deviation at 2 μm. The largest final deviation reported is 0.0123mm, which is a 94.7% decrease in the maximum deviation between the steps of the algorithm. This deviation is likely driven primarily by generation of the underlying .stl files, which were created with a tolerance of

5 μm. The large variation in results between the ICP registration and the final registration indicate that rigid alignment of the nominal model and actual probed geometry is not sufficient to accurately reconstruct a geometry to be repaired and shows the impact of the mean line registration.

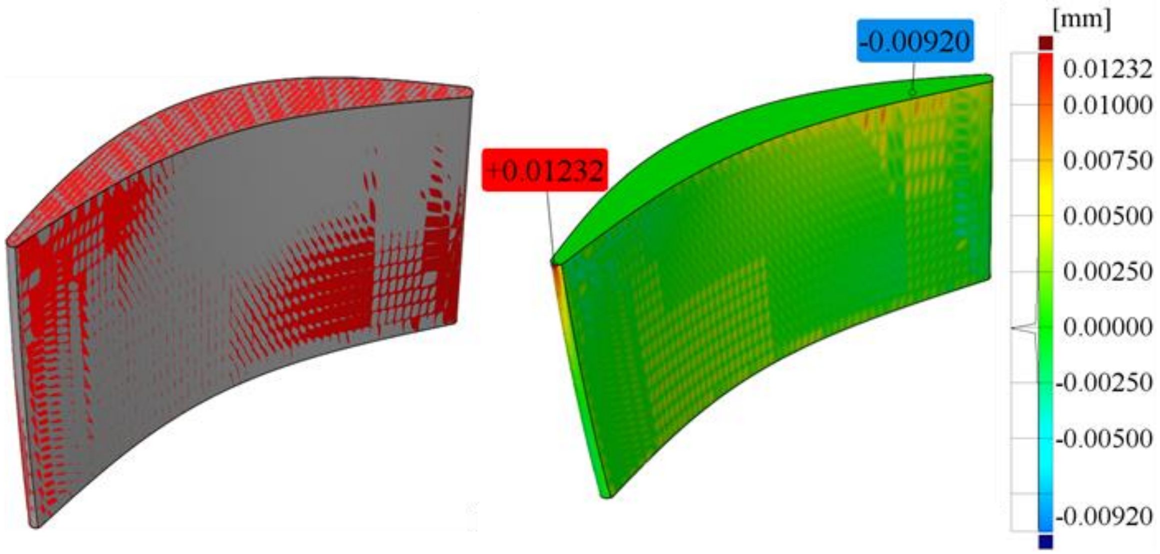

Figure 16: Surface comparison: (a) Final transformed nominal in grey with actual data shown in red (b) deviation map

Table 1: Surface comparison results for ICP and final registration

Sample	Max. (mm)	Min. (mm)	Mean (mm)	σ (mm)
ICP surface comparison	0.2343	-0.2047	0.0400	0.0325
Final surface comparison	0.0123	-0.0092	-0.0003	0.0020
Delta	0.2220	0.1955	0.0397	0.0305

Table 2: Surface comparison results from four samples

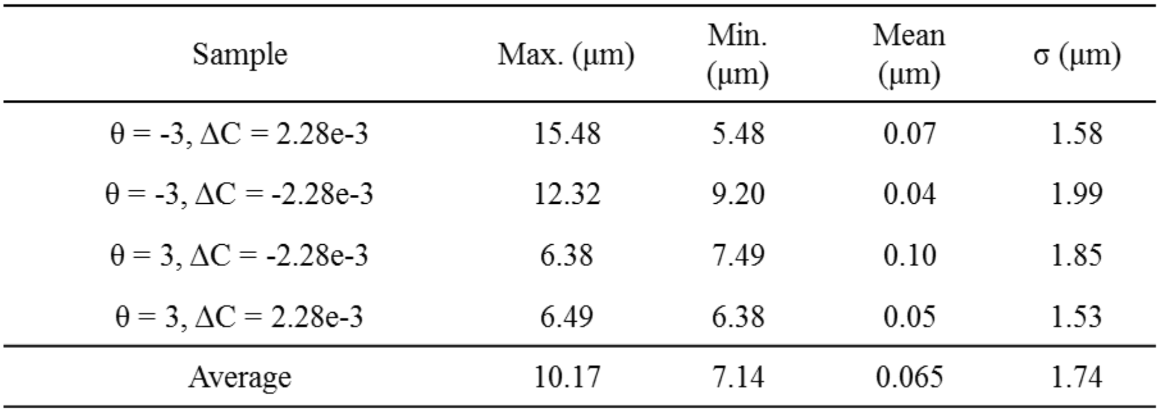

Sample	Max. (µm)	Min. (µm)	Mean (µm)	σ (µm)
θ = -3, ΔC = 2.28e-3	15.48	5.48	0.07	1.58
θ = -3, ΔC = -2.28e-3	12.32	9.20	0.04	1.99
θ = 3, ΔC = -2.28e-3	6.38	7.49	0.10	1.85
θ = 3, ΔC = 2.28e-3	6.49	6.38	0.05	1.53
Average	10.17	7.14	0.065	1.74

The surface comparison results for three other samples with θ values of ±.118 °/mm and ΔC values of ±2.28e-3 mm/mm can be seen in Table 2. A mean deviation of 0.065 µm across all samples was found, confirming the accuracy of the model for the majority of the blade geometry. The maximum profile deviation of 15.480 µm was observed for a deformation condition of θ = -0.118 °/mm, ΔC = 2.28e-3 mm/mm, which were the extremum for deformations examined. The location of the maximum profile deviation occurred in the repair region for all deformation conditions. This is generally expected, as the final profile's transformations are computed via interpolation from the profiles in the non-repair region. However, these maximum values appear far beyond the 6σ bounds around the mean, where the average standard deviation of these measured values was found to be 1.74 µm, showing that these values do not reflect the overall quality of the registration. The overall impact of these maximum values on the blend process is minimal, however, as this is not critical to the interface between the repair region and parent (non-repair) region surface.

4.1.2 *Evaluation of algorithm in blend region*

During the part repair process, the repaired region needs to be constructed. However, while the majority of this region is contained entirely within the deposition stage and can be machined to any prescribed geometry, the lower portion of this region is required to blend smoothly with the parent material. Therefore, it is imperative that the algorithm accurately reconstructs the geometry where the parent region meets the repaired region material. In order to test this, additively repaired geometries were created for the maximum conditions observed in this study with the following conditions: $\theta = \pm 0.118$ °/mm and ΔC values of $\pm 2.28e\text{-}3$ mm/mm. The repair algorithm was used to transform the nominal geometries and a surface comparison was then performed to analyze the differences between registered regions.

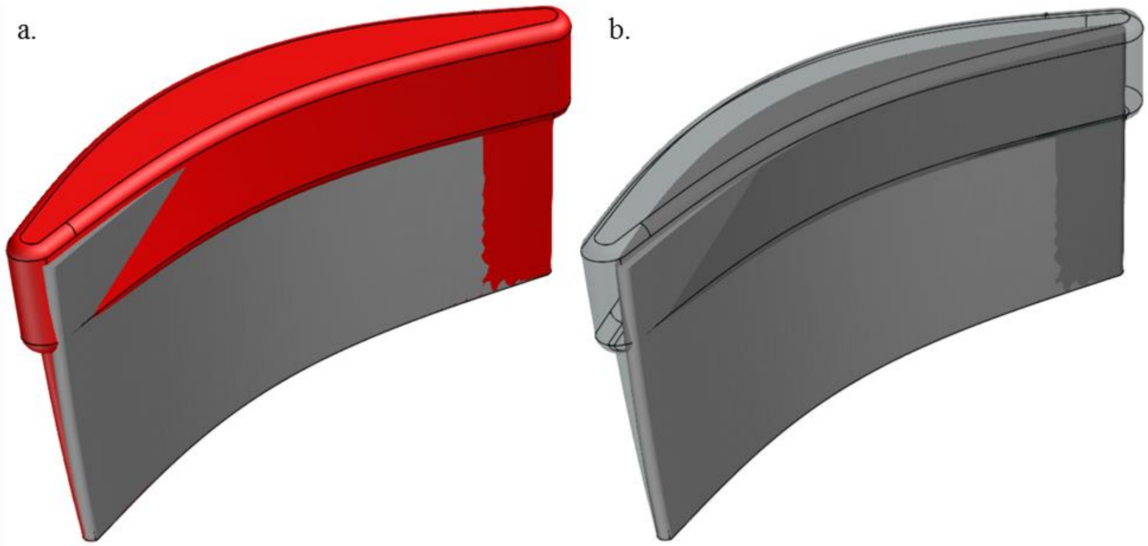

Figure 17: An actual blade (red) with deformation parameters $\theta = -.118$ °/mm, $\Delta C = -2.28e\text{-}3$ mm/mm compared with the nominal geometry (grey). Actual blade shown opaque in (a.) and transparent in (b.)

An example of one of these geometries is shown in Figure 17. The nominal geometry is shown in grey prior to any adaptation. The actual geometry, created with deformation parameters θ = -0.118 °/mm, ΔC = -2.28e-3 mm/mm, is shown in red in Figure 17(a), and shown transparent in Figure 17(b), showing a lack of alignment throughout the model. Because of the deformation parameters used, it can be seen that the nominal model no longer matches the actual geometry, and a comparison of these two blades can be seen without the deposition in Figure 14(a). While this deformation may not appear as significant in Figure 14 (a), Figure 17 (a) shows that these deformation values are significant enough to transform the blade tip outside of the repair volume. Because of this, an attempt at non-adaptive repair based on the nominal repair process executed on this component would fail.

Figure 18(a) depicts Figure 17(a) from another angle, coloring the nominal model blue for clarity. Figure 18(b) depicts the same comparison after the completion of the registration process. The new transformed model now lies entirely within the envelope of

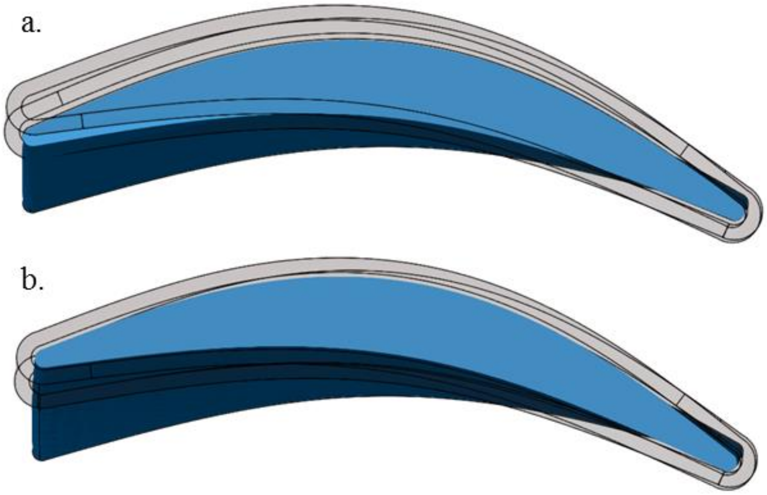

Figure 18: Nominal model (blue) depicted relative to welded actual geometry before (a.) and after (b.) registration

the additively repaired geometry, making this component repairable with machining processes based off of the registered nominal. However, the quality of registration within the blend area must also be examined to ensure accurate registration of the nominal.

Figure 19 demonstrates the results for the same deformation condition with geometric deformation parameters of θ = -0.118 °/mm, ΔC = -2.28e-3 mm/mm. The maximum deviation for the final registration in this region was found to be 3.6 μm, shown in Table 3, and occurred at the base of the additive repair region interface with the parent material. The location of this maximum deviation is expected, as any geometry created past the Kth probed section is highly dependent on the interpolated final profile. However, the mean deviation found in this comparison was 0.08 μm, with a standard deviation of 0.69 μm. These values are significantly smaller that the values listed in Table 1 and Table 2 for the full model surface comparisons. This shows that the majority of deviation occurs with the portion of the model to be machined from the additive repair region and not at the blend region between the repair and the parent material.

Table 3: Blend region surface comparison results

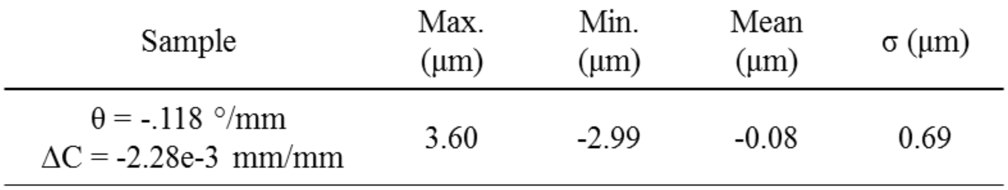

Sample	Max. (μm)	Min. (μm)	Mean (μm)	σ (μm)
θ = -.118 °/mm ΔC = -2.28e-3 mm/mm	3.60	-2.99	-0.08	0.69

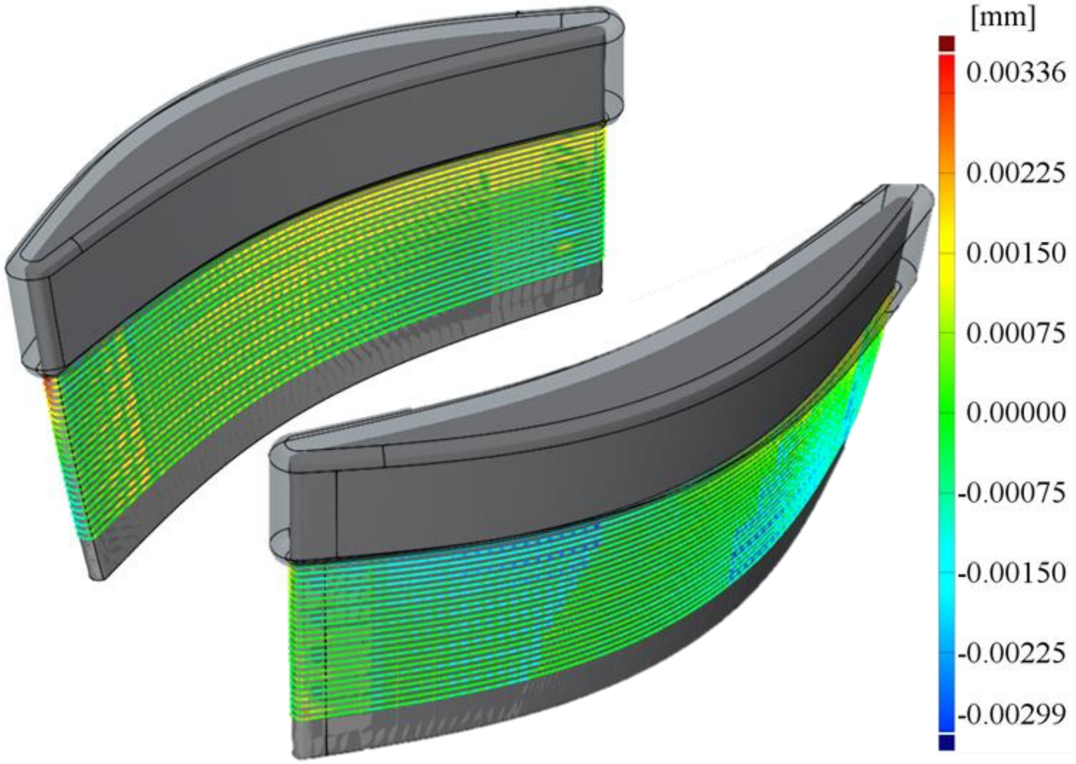

Figure 19: Surface comparison of completely registered blade (opaque) to actual welded geometry (transparent) shown from multiple angles

4.2 Evaluation of potential benefits and gains

The previous results have shown that this algorithm is capable of accurately manipulating the CAD geometry of a nominal model to match the geometry of a part that has experienced deformation in service. In use, this algorithm could be used to create models of the actual blade for use in both the additive and subtractive phases of the repair process. In the additive phase this model can adapt the geometry of material to be deposited, and in the subtractive phase to adapt the blade geometry as shown previously.

4.2.1 Material efficiency evaluations

During a tip repair, the damaged blade tip is first removed from the blade via machining. Material is then deposited using a welding process to rebuild material in the repair area. This material deposition is completed using a previously calculated path derived from the nominal CAD geometry of the blade. However, due to variations in blade geometry associated with deformation throughout use of the component, this static path may not be effective as: (1) it may not deposit a sufficient margin of material to successfully machine the component in later phases of the repair, (2) it may be inefficient in terms of material efficiency. The results of the former case are shown in Figure 20(a), where the additive deposition path did not provide an adequate margin of material between the weld envelope and the intended final part geometry. This can be mitigated by increasing the thickness of the deposited weld bead along the nominal path. However, a naïve approach such as this would introduce an uneven margin of material between the deposited weld and the intended final part geometry. This material inefficiency is evident in Figure 20(b), where the weld thickness has been increased to meet the minimum required margin of

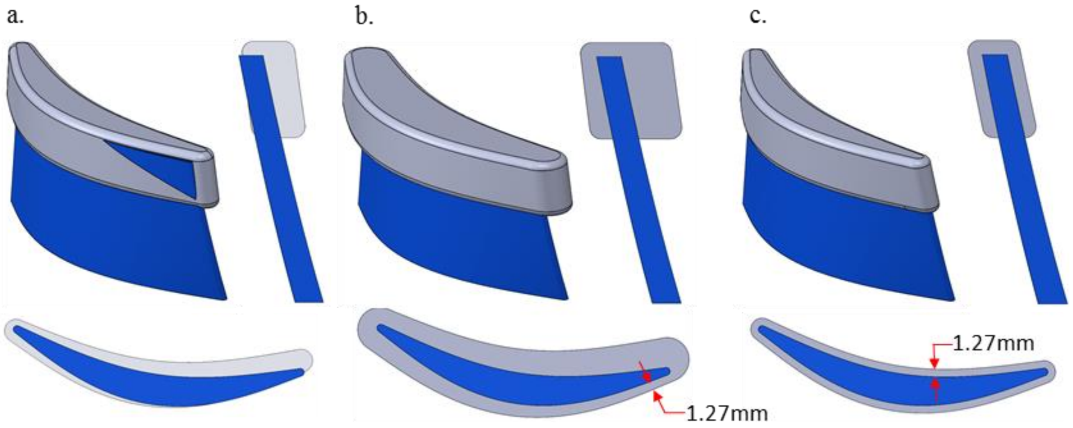

Figure 20: Weld profiles superimposed on an actual geometry (a) created from the nominal data (b) created by increasing the offset of nominal weld (c) weld created using adaptive geometry. Images of two different cross sections are shown for each profile.

material. To combat this inefficiency in the naïve approach, an adaptation of the deposited repair geometry could be made following the adaptive registration algorithm described above. Figure 20(c) shows the result in the case where the repair geometry for each blade is adapted using the previously described algorithm using an identical minimum margin requirement as in Figure 20(b).

To determine the potential material savings using an adaptive additive repair method, 35 actual blade models were created using the factors listed in Table 4. Each model was input into the algorithm to create a deformed nominal model for each. Adaptive weld geometries for each sample were created by adding a margin of 1.27 mm to the thickness distribution of each blade during the profile creation process to allow an adequate margin for the subsequent machining process. These surfaces were then trimmed at consistent heights, closed with planar surfaces, and filleted to create solid geometries. Non-adaptive blades were then created by increasing the thickness of the nominal weld until the minimum distance between the weld and intended part geometry reached the required margin of 1.27 mm.

Table 4: Blade create parameters used in efficiency evaluation

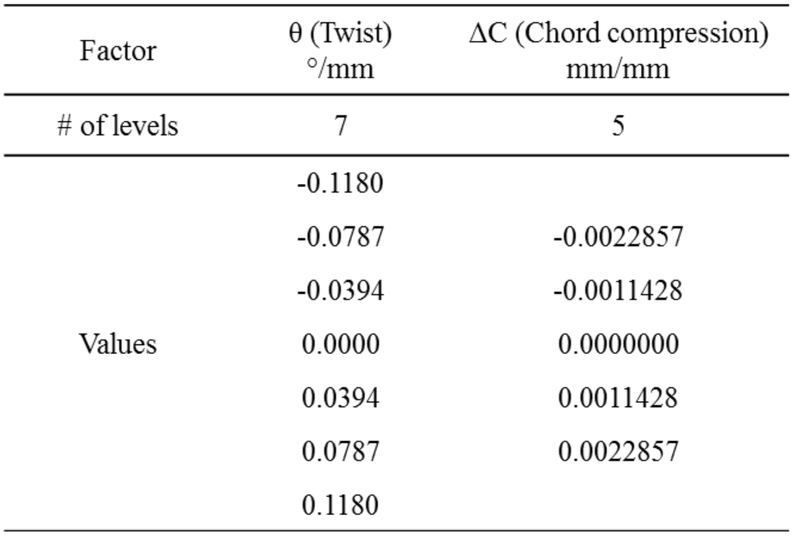

Factor	θ (Twist) °/mm	ΔC (Chord compression) mm/mm
# of levels	7	5
Values	-0.1180	
	-0.0787	-0.0022857
	-0.0394	-0.0011428
	0.0000	0.0000000
	0.0394	0.0011428
	0.0787	0.0022857
	0.1180	

For each sample, a material efficiency was calculated by dividing the nominal weld volume by the respective sample volumes for both the adaptive and non-adaptive weld generation process. Figure 21 shows the material efficiency compared to the nominal weld volume for all samples. As expected, more weld volume is required during the non-adaptive process as the actual blade geometry varies increasingly farther from the nominal blade. From the figure, both types of geometry changes (twist and chord length) have an effect on the material efficiency of the weld deposition, however blade twist has a much more significant effect for the values in the present study. At its maximum value of $\Delta C = 0.0022857$ mm/mm, changes in chord length alone only saw a decrease in efficiency of 3.6%. This is compared to a 42.2% decrease in efficiency seen in a model with the maximum value of twist $\theta = 0.1180$ °/mm. In comparison, the material efficiency of the adaptive process remains very close to 100% for all samples. In fact, the lowest efficiency

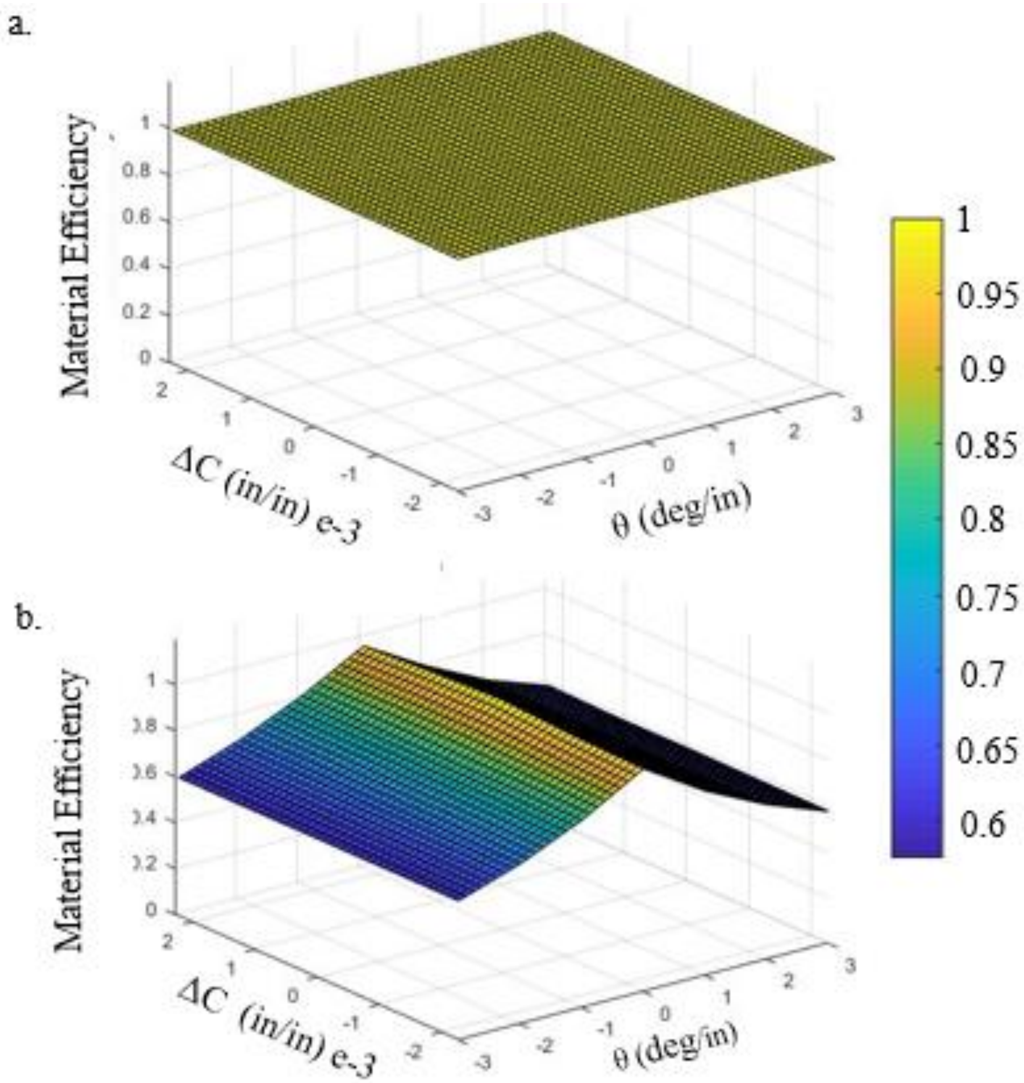

Figure 21: Comparison of adaptive (a.) and non-adaptive (b.) material efficiency in the weld deposition process with respect to changes in Twist (θ) and Chord compression (ΔC).

recorded in the adaptive process was 99.2%, which occurred at a θ = -0.1180 °/mm and ΔC = -0.0022857 mm/mm.

These results show the potential for significant material savings in the additive deposition phase. If this process were implemented in a hybrid system using a powder based directed energy deposition, these could transfer to significant cost savings. The volume for the nominal weld 2.715 cm^3. Using the density of Inconel 718 as 8.74 g/cm^3

and the cost per kilogram of powder as $200, the nominal material cost for the weld would be $4.75 [20, 69]. Given the 35 blade geometries examined in this study, the total savings by implementing the adaptive strategy would total $65.94, allowing for the creation of 13 addition welds.

4.2.2 Machining time and material removal simulations

The previously discussed non-adaptive deposition strategy affects not only the material efficiency associated with additive processing in a repair, but also affects the subsequent machining processes. To evaluate the effect of a chosen deposition process on machining process efficiency, the differences in calculated machining time to complete the repair process between the adaptive and non-adaptive deposition strategies were inspected, where the primary differences lie in the time required to remove superfluous material in the non-adaptive deposition process. Figure 22 shows the steps taken in the machining simulations and were generated using a 5-axis CAM software [70]. This involves the following elements: a 3-axis roughing pass to intermediate geometry in Figure 20(a), a pre-finishing pass utilizing 5-axis toolpaths to reduce the repair region to a uniform margin in

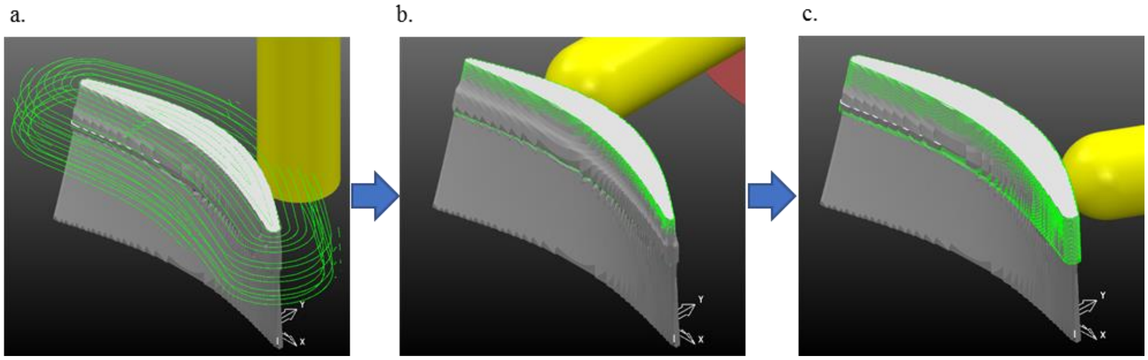

Figure 22: Images of tool path strategies used in machining simulations, roughing (a.), pre-finishing (b.), and finishing (c.)

Table 5: Machining simulation parameters

	Roughing	Finishing
Tool	6 Flute, .5” End Mill	4 Flute, .5” Ball mill
Speed (SFM)	200	200
Feed (in/Tooth)	0.001	0.001
Stepover (in)	0.05	0.01
Stepdown (in)	0.1	-

Figure 20(b), and a final finishing pass utilizing 5-axis toolpaths to bring the part geometry to its final state in Figure 20(c).

The machining parameters and tools associated with each of these toolpaths are shown in Table 5, and are parameters for machining Inconel 718, a common airfoil alloy [71]. These machining parameters also agree with tooling manufacturer specifications for similar tools used in nickel based superalloy materials [72]. For each sample, the time required to complete each of the individual machining operation was recorded, along with the volume of material removed during the operation. Figure 23 shows the resulting

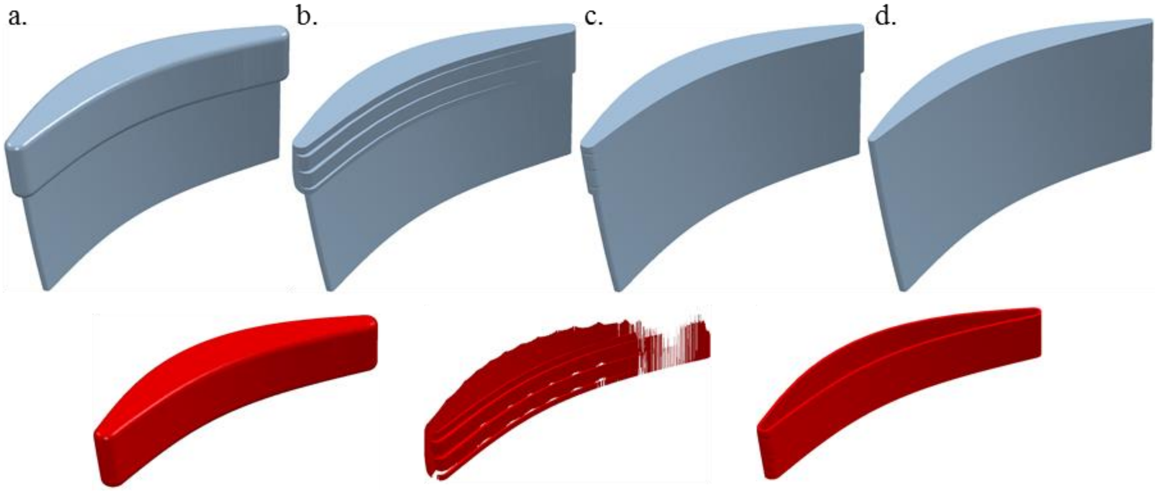

Figure 23: Effect of subsequent passes on the initial volume. Shown in grey is the part after each step, with the material removed during machining shown in red.

Table 6: Machining simulation results for parameters θ = -0.118, ΔC = -2.28e-3

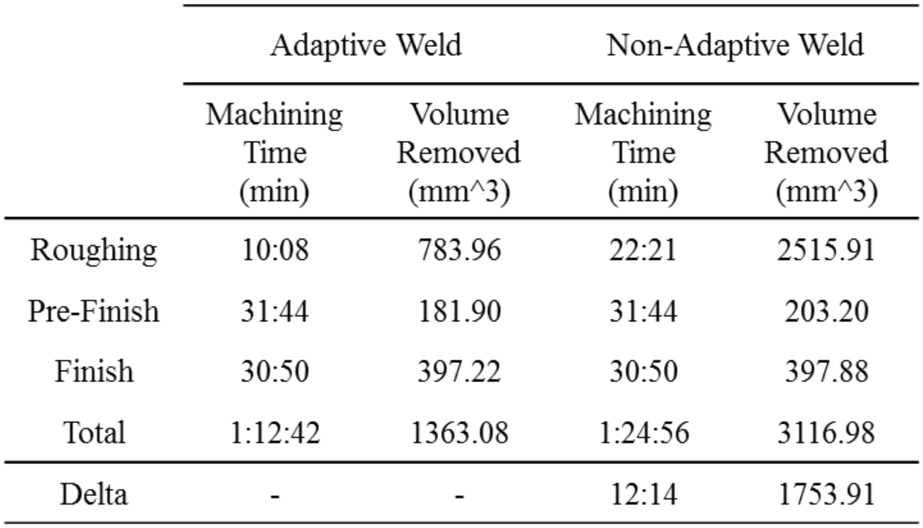

	Adaptive Weld		Non-Adaptive Weld	
	Machining Time (min)	Volume Removed (mm^3)	Machining Time (min)	Volume Removed (mm^3)
Roughing	10:08	783.96	22:21	2515.91
Pre-Finish	31:44	181.90	31:44	203.20
Finish	30:50	397.22	30:50	397.88
Total	1:12:42	1363.08	1:24:56	3116.98
Delta	-	-	12:14	1753.91

geometry created throughout this machining strategy. The material removed in each step of the machining strategy shown in Figure 22 is shown in red in Figure 23. These volumes were used to assess the difference in material removal between the adaptive and non-adaptive material deposition strategies. Table 6 details the results from these machining simulations for sample generated with parameters θ = -0.118 °/mm, ΔC = -2.28e-3 mm/mm. The adaptive deposition strategy and subsequent adaptive machining strategy shows a significant enhancement of 12:14 total minutes saved in the machining process. Table 6 also details the material volume removed in two repair strategies, and which individual steps in the process see the greatest change in material removal. From the table, while the process times for the pre-finish and finish passes remain unchanged, the roughing process sees a significant decrease of 12:13 minutes, which is approximately 14% of the total machining time in the non-adaptive process. This directly shows the time required to process the excess material deposited during the non-adaptive deposition strategy. The roughing pass also shows the largest change in volume of material removed with 1731.95 mm^3 removed in the non-adaptive strategy. However, the pre-finishing tool path also shows an increase in material removed. This is due to an increase in material lying under overhanging regions which are inaccessible to the three-axis roughing process. This excess material must then be removed in the 5-axis pre-finishing process. As expected, the finishing process sees no change in either machining time or material removed, as it based on the final geometry which does not change for either strategy.

To further investigate these effects, these machining simulations were completed on ten separate samples with varying levels twist and chord change. Table 7 shows the total change in machining time to removed welds created in the adaptive and non-adaptive weld deposition strategies. For each of the samples tested, significant decreases in the machining time were realized as a result of the adaptive weld deposition strategy. A minimum of 9 minutes of machining time was reduced from all samples, which is approximately a 10% decrease in machining time for this process.

Table 7: Machining simulation results for 10 samples with indicated conditions

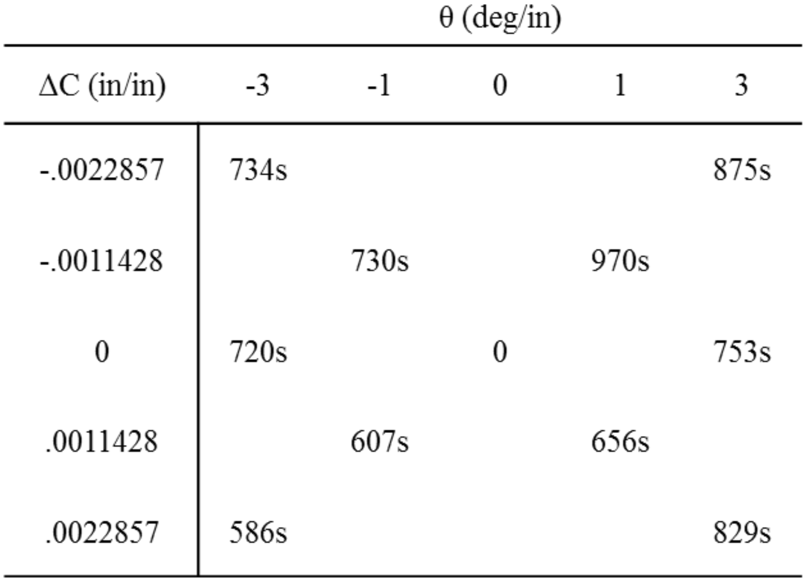

	θ (deg/in)				
ΔC (in/in)	-3	-1	0	1	3
-.0022857	734s				875s
-.0011428		730s		970s	
0	720s		0		753s
.0011428		607s		656s	
.0022857	586s				829s

CHAPTER 5. CONCLUSION

This chapter summarizes the original contributions and main conclusions of this these and suggests possible areas for future study.

5.1 Original Contributions

In this work, an adaptive registration method for the repair of high value components has been presented, which is capable of execution within the framework of a commercial hybrid manufacturing system. This method provides a unique formulation for the registration and interpolation of dense point samples to distort a nominal model. This method is designed to function in the environment of a commercial hybrid manufacturing system, utilizing data acquisition from only strain gauge style measurement probes, which is previously undiscussed. This work also presents a case study to evaluate the potential efficiency gains by utilizing an adaptive process within a hybrid framework.

5.2 Main Conclusions

In this work, a method for adaptive geometry transformation which could be implemented in a single setup for hybrid manufacturing machines was presented. In initial tests, profile based rigid registration proved to show an accurate first alignment of the model. The mean line transformation method was then shown to remove any profile-based deformation which may occur. In surface comparison results, transformed nominal models were shown to match the actual component geometry. Over samples tested a maximum deviation of 15.480 μm was observed within the repair region near the tip of the samples. With mean and standard deviation values of 0.065 μm and 1.740 μm respectively, the overall surface registration showed accurate alignment. However, in the case of blending for a blade repair, the maximum deviation seen in the transition region between the manipulated CAD and the actual blade was shown to be only 3.6 μm, with a mean deviation of the blend region of 0.08 μm. These results show adequate surface accuracy for use in a blade repair process. By utilizing this adaptive method in a commercial hybrid manufacturing system with control over both the additive and subtractive phases of the process, significant process savings can be realized. In the additive deposition phase, it was shown that an adaptive strategy's efficiency increases over a naïve strategy as part deformation increases. At the extremum of deformations sampled, a material savings of 42.4% was realized. These savings have been shown not only in material savings in the deposition phase, but also in process time in the finish machining stage. By using the adaptive deposition strategy, machining time savings up to 16 minutes were shown, with savings of at least 9 minutes shown for all samples tested.

5.3 Recommendations for future study

Simulations presented here were developed using surrogate models for a repair process. Because of this, many questions can still be answered. Since the actual models in this study were also constructed, no errors in data acquisition are present. Characterization of deformation on actual components could also lead to different interpretations in the algorithm. Different deformation trends along actual components can be detected by changing the interpolation function for the final profile, as previously stated. However, the effects of the introduction of sampling noise and density of sampled points along the cross section are currently unknown. These effects could be shown in simulation. However, to fully understand possible sources of error in this framework, full integration with a hybrid machine, including the exchange of on machine inspection data and adaptive creation of additive and subtractive toolpaths, should be investigated. In the remanufacture of these components, the final repaired component must be verified for compliance with dimensional specifications. Therefore, tolerance-based constraints would need to be integrated into the model to ensure that an out-of-spec component cannot be produced. However, this could simply be done by constraint of the transformation and deformation ranges of the final profile.

REFERENCES

[1] R. Vilar, "Laser cladding," *Journal of laser applications,* vol. 11, no. 2, pp. 64-79, 1999.

[2] K. Mumtaz and N. Hopkinson, "Top surface and side roughness of Inconel 625 parts processed using selective laser melting," (in English), *Rapid Prototyping Journal,* vol. 15, no. 2, pp. 96-103, 2009.

[3] J. Kranz, D. Herzog, and C. Emmelmann, "Design guidelines for laser additive manufacturing of lightweight structures in TiAl6V4," (in English), *Journal of Laser Applications,* vol. 27, no. S1, p. S14001, Feb 2015.

[4] J. Kruth, B. Vandenbroucke, J. Van Vaerenbergh, and P. Mercelis, "Benchmarking of different SLS/SLM processes as rapid manufacturing techniques," *Laser,* vol. 1, p. 3D, 2005.

[5] P. Das, R. Chandran, R. Samant, and S. Anand, "Optimum Part Build Orientation in Additive Manufacturing for Minimizing Part Errors and Support Structures," (in English), *43rd North American Manufacturing Research Conference, Namrc 43,* vol. 1, pp. 343-354, 2015.

[6] M. Zhou, J. Xi, and J. Yan, "Adaptive direct slicing with non-uniform cusp heights for rapid prototyping," *The International Journal of Advanced Manufacturing Technology,* vol. 23, no. 1-2, pp. 20-27, 2004.

[7] M. B. Bauza *et al.*, "Study of accuracy of parts produced using additive manufacturing," Lawrence Livermore National Laboratory (LLNL), Livermore, CA2014.

[8] R. Paul, S. Anand, and F. Gerner, "Effect of Thermal Deformation on Part Errors in Metal Powder Based Additive Manufacturing Processes," (in English), *Journal of Manufacturing Science and Engineering-Transactions of the Asme,* vol. 136, no. 3, p. 031009, Jun 2014.

[9] R. Wauthle *et al.*, "Effects of build orientation and heat treatment on the microstructure and mechanical properties of selective laser melted Ti6Al4V lattice structures," *Additive Manufacturing,* vol. 5, pp. 77-84, 2015.

[10] B. Vrancken, V. Cain, R. Knutsen, and J. Van Humbeeck, "Residual stress via the contour method in compact tension specimens produced via selective laser melting," (in English), *Scripta Materialia,* vol. 87, pp. 29-32, Sep 15 2014.

[11] J. Laeng, J. G. Stewart, and F. W. Liou, "Laser metal forming processes for rapid prototyping - a review," (in English), *International Journal of Production Research,* vol. 38, no. 16, pp. 3973-3996, Nov 10 2000.

[12] O. Oyelola, P. Crawforth, R. M'Saoubi, and A. T. Clare, "Machining of Additively Manufactured Parts: Implications for Surface Integrity," (in English), *3rd Cirp Conference on Surface Integrity*, vol. 45, pp. 119-122, 2016.

[13] S. Rawal, J. Brantley, and N. Karabudak, "Additive manufacturing of Ti-6Al-4V alloy components for spacecraft applications," in *Recent Advances in Space Technologies (RAST), 2013 6th International Conference on*, 2013, pp. 5-11: IEEE.

[14] S. W. Williams, F. Martina, A. C. Addison, J. Ding, G. Pardal, and P. Colegrove, "Wire+ arc additive manufacturing," *Materials Science and Technology,* vol. 32, no. 7, pp. 641-647, 2016.

[15] M. K. Thompson *et al.*, "Design for Additive Manufacturing: Trends, opportunities, considerations, and constraints," (in English), *Cirp Annals-Manufacturing Technology,* vol. 65, no. 2, pp. 737-760, 2016.

[16] B. Lauwers, F. Klocke, A. Klink, A. E. Tekkaya, R. Neugebauer, and D. Mcintosh, "Hybrid processes in manufacturing," (in English), *Cirp Annals-Manufacturing Technology,* vol. 63, no. 2, pp. 561-583, 2014.

[17] S. Simhambhatla and K. P. Karunakaran, "Build strategies for rapid manufacturing of components of varying complexity," (in English), *Rapid Prototyping Journal,* vol. 21, no. 3, pp. 340-350, 2015.

[18] J. Zhang and F. Liou, "Adaptive slicing for a multi-axis laser aided manufacturing process," (in English), *Journal of Mechanical Design,* vol. 126, no. 2, pp. 254-261, Mar 2004.

[19] M. Soshi, J. Ring, C. Young, Y. Oda, and M. Mori, "Innovative grid molding and cooling using an additive and subtractive hybrid CNC machine tool," (in English), *Cirp Annals-Manufacturing Technology,* vol. 66, no. 1, pp. 401-404, 2017.

[20] T. Yamazaki, "Development of a hybrid multi-tasking machine tool: integration of additive manufacturing technology with CNC machining," *Procedia CIRP,* vol. 42, pp. 81-86, 2016.

[21] S. T. Newman, Z. C. Zhu, V. Dhokia, and A. Shokrani, "Process planning for additive and subtractive manufacturing technologies," (in English), *Cirp Annals-Manufacturing Technology,* vol. 64, no. 1, pp. 467-470, 2015.

[22] L. Ren, T. Sparks, J. Z. Ruan, and F. Liou, "Integrated Process Planning for a Multiaxis Hybrid Manufacturing System," (in English), *Journal of Manufacturing Science and Engineering-Transactions of the Asme,* vol. 132, no. 2, p. 021006, Apr 2010.

[23] J. Wang, S. Prakash, Y. Joshi, and F. Liou, "Laser aided part repair-a review," 2002: Citeseer.

[24] J. B. Jones, P. McNutt, R. Tosi, C. Perry, and D. I. Wimpenny, "Remanufacture of turbine blades by laser cladding, machining and in-process scanning in a single machine," in *23rd annual internationalsolid freeform fabrication symposium*, 2012, pp. pp.821–827, Austin,TX, USA, 2012.

[25] L. Ren, A. P. Padathu, J. Ruan, T. Sparks, and F. W. Liou, "Three dimensional die repair using a hybrid manufacturing system," *Austin, TX*, 2008.

[26] D.-S. Choi *et al.*, "Development of a direct metal freeform fabrication technique using CO2 laser welding and milling technology," *Journal of Materials Processing Technology,* vol. 113, no. 1-3, pp. 273-279, 2001.

[27] K. Karunakaran, S. Suryakumar, V. Pushpa, and S. Akula, "Retrofitment of a CNC machine for hybrid layered manufacturing," *The International Journal of Advanced Manufacturing Technology,* vol. 45, no. 7, pp. 690-703, 2009.

[28] J. M. Flynn, A. Shokrani, S. T. Newman, and V. Dhokia, "Hybrid additive and subtractive machine tools–Research and industrial developments," *International Journal of Machine Tools and Manufacture,* vol. 101, pp. 79-101, 2016.

[29] Hermle. (2016, 4/19/2018). *MPA - A metal powder application technique*. Available: http://www.hermle-generativ-fertigen.de/cms/en/technology/

[30] A. Hansel *et al.*, "Study on consistently optimum deposition conditions of typical metal material using additive/subtractive hybrid machine tool," (in English), *7th Hpc 2016 - Cirp Conference on High Performance Cutting,* vol. 46, pp. 579-582, 2016.

[31] Renishaw. *SPRINT™ on-machine contact scanning system*. Available: http://www.renishaw.com/en/sprint-on-machine-contact-scanning-system--20908

[32] B. Bellekens, V. Spruyt, R. Berkvens, and M. Weyn, "A survey of rigid 3d pointcloud registration algorithms," in *AMBIENT 2014: the Fourth International Conference on Ambient Computing, Applications, Services and Technologies, August 24-28, 2014, Rome, Italy*, 2014, pp. 8-13.

[33] C. R. Maurer, J. M. Fitzpatrick, M. Y. Wang, R. L. Galloway, R. J. Maciunas, and G. S. Allen, "Registration of head volume images using implantable fiducial markers," *IEEE transactions on medical imaging,* vol. 16, no. 4, pp. 447-462, 1997.

[34] K. S. Arun, T. S. Huang, and S. D. Blostein, "Least-squares fitting of two 3-d point sets," *IEEE Trans Pattern Anal Mach Intell,* vol. 9, no. 5, pp. 698-700, May 1987.

[35] S. Oomori, T. Nishida, and S. Kurogi, "Point cloud matching using singular value decomposition," (in English), *Artificial Life and Robotics,* vol. 21, no. 2, pp. 149-154, Jun 2016.

[36] S. Wold, K. Esbensen, and P. Geladi, "Principal Component Analysis," (in English), *Chemometrics and Intelligent Laboratory Systems,* vol. 2, no. 1-3, pp. 37-52, Aug 1987.

[37] G. F. Byrne, P. F. Crapper, and K. K. Mayo, "Monitoring Land-Cover Change by Principal Component Analysis of Multitemporal Landsat Data," (in English), *Remote Sensing of Environment,* vol. 10, no. 3, pp. 175-184, 1980.

[38] W. S. Yambor, B. A. Draper, and J. R. Beveridge, "Analyzing PCA-based face recognition algorithms: Eigenvector selection and distance measures," in *Empirical evaluation methods in computer vision*: World Scientific, 2002, pp. 39-60.

[39] A. Weckenmann *et al.*, "Multisensor data fusion in dimensional metrology," (in English), *Cirp Annals-Manufacturing Technology,* vol. 58, no. 2, pp. 701-721, 2009.

[40] P. J. Besl and N. D. McKay, "A method for registration of 3-D shapes," *IEEE Transactions on pattern analysis and machine intelligence,* vol. 14, no. 2, pp. 239-256, 1992.

[41] Y. Chen and G. Medioni, "Object Modeling by Registration of Multiple Range Images," (in English), *Image and Vision Computing,* vol. 10, no. 3, pp. 145-155, Apr 1992.

[42] Z. Y. Zhang, "Iterative Point Matching for Registration of Free-Form Curves and Surfaces," (in English), *International Journal of Computer Vision,* vol. 13, no. 2, pp. 119-152, Oct 1994.

[43] R. Bergevin, M. Soucy, H. Gagnon, and D. Laurendeau, "Towards a general multi-view registration technique," (in English), *Ieee Transactions on Pattern Analysis and Machine Intelligence,* vol. 18, no. 5, pp. 540-547, May 1996.

[44] K. Pulli, "Multiview registration for large data sets," in *3-D Digital Imaging and Modeling, 1999. Proceedings. Second International Conference on*, 1999, pp. 160-168: IEEE.

[45] G. Turk and M. Levoy, "Zippered polygon meshes from range images," in *Proceedings of the 21st annual conference on Computer graphics and interactive techniques*, 1994, pp. 311-318: ACM.

[46] S. Fantoni, U. Castellani, and A. Fusiello, "Accurate and automatic alignment of range surfaces," in *3D Imaging, Modeling, Processing, Visualization and Transmission (3DIMPVT), 2012 Second International Conference on*, 2012, pp. 73-80: IEEE.

[47] M. A. Audette, F. P. Ferrie, and T. M. Peters, "An algorithmic overview of surface registration techniques for medical imaging," *Med Image Anal,* vol. 4, no. 3, pp. 201-17, Sep 2000.

[48] B. Allen, B. Curless, and Z. Popović, "The space of human body shapes: reconstruction and parameterization from range scans," *ACM transactions on graphics (TOG),* vol. 22, no. 3, pp. 587-594, 2003.

[49] B. J. Brown and S. Rusinkiewicz, "Global non-rigid alignment of 3-D scans," in *ACM Transactions on Graphics (TOG)*, 2007, vol. 26, no. 3, p. 21: ACM.

[50] M. Weinstein, "Remanufacture of Jet Engine Compressor Components," in *ASME 1973 International Gas Turbine Conference and Products Show*, 1973, pp. V001T01A043-V001T01A043: American Society of Mechanical Engineers.

[51] O. Rupp, "Instandhaltungskosten bei zivilen Strahltriebwerken," in *Deutscher Luft- und Raumfahrtkongress*, 2001, pp. 2001-008.

[52] A. Hamed, W. Tabakoff, and R. Wenglarz, "Erosion and deposition in turbomachinery," (in English), *Journal of Propulsion and Power,* vol. 22, no. 2, pp. 350-360, Mar-Apr 2006.

[53] B. Denkena, V. Boess, D. Nespor, F. Floeter, and F. Rust, "Engine blade regeneration: a literature review on common technologies in terms of machining," *The International Journal of Advanced Manufacturing Technology*, vol. 81, no. 5-8, pp. 917-924, 2015.

[54] C. Bremer, "Automated repair and overhaul of aero-engine and industrial gas turbine components," in *ASME Turbo Expo 2005: Power for Land, Sea, and Air*, 2005, pp. 841-846: American Society of Mechanical Engineers.

[55] C. Bremer, "Data Management and Adaptive Machining Technology for Efficient Repair and Manufacture of Turbine Components," in *ASME Turbo Expo 2008: Power for Land, Sea, and Air*, 2008, pp. 415-422: American Society of Mechanical Engineers.

[56] H. Qi, M. Azer, and P. Singh, "Adaptive toolpath deposition method for laser net shape manufacturing and repair of turbine compressor airfoils," (in English), *International Journal of Advanced Manufacturing Technology,* vol. 48, no. 1-4, pp. 121-131, Apr 2010.

[57] P. Singh, H. Qi, M. N. Azer, and P. M. Kulkarni, "Laser net shape manufacturing and repair using a medial axis toolpath deposition method," ed: Google Patents, 2008.

[58] J. M. Zheng, Z. G. Li, and X. Chen, "Worn area modeling for automating the repair of turbine blades," (in English), *International Journal of Advanced Manufacturing Technology,* vol. 29, no. 9-10, pp. 1062-1067, Jul 2006.

[59] O. Yilmaz, N. Gindy, and J. Gao, "A repair and overhaul methodology for aeroengine components," (in English), *Robotics and Computer-Integrated Manufacturing,* vol. 26, no. 2, pp. 190-201, Apr 2010.

[60] Z. Yun, C. Zhi-Tong, and N. Tao, "Reverse modeling strategy of aero-engine blade based on design intent," (in English), *International Journal of Advanced Manufacturing Technology,* vol. 81, no. 9-12, pp. 1781-1796, Dec 2015.

[61] Y. Dong, D. Zhang, K. Bu, Y. Dou, and W. Wang, "Geometric parameter-based optimization of the die profile for the investment casting of aerofoil-shaped turbine blades," *The International Journal of Advanced Manufacturing Technology,* vol. 57, no. 9-12, p. 1245, 2011.

[62] Y. Rong, J. Xu, and Y. Sun, "A surface reconstruction strategy based on deformable template for repairing damaged turbine blades," *Proceedings of the Institution of Mechanical Engineers, Part G: Journal of Aerospace Engineering,* vol. 228, no. 12, pp. 2358-2370, 2014.

[63] Y. L. Ke, S. Q. Fan, W. D. Zhu, A. Li, F. S. Liu, and X. Q. Shi, "Feature-based reverse modeling strategies," (in English), *Computer-Aided Design,* vol. 38, no. 5, pp. 485-506, May 2006.

[64] Y. Q. Li and J. Ni, "Constraints Based Nonrigid Registration for 2D Blade Profile Reconstruction in Reverse Engineering," (in English), *Journal of Computing and Information Science in Engineering,* vol. 9, no. 3, p. 031005, Sep 2009.

[65] E. Bagci, "Reverse engineering applications for recovery of broken or worn parts and re-manufacturing: Three case studies," *Advances in Engineering Software,* vol. 40, no. 6, pp. 407-418, 2009.

[66] J. Gao, A. Folkes, O. Yilmaz, and N. Gindy, "Investigation of a 3D non-contact measurement based blade repair integration system," (in English), *Aircraft Engineering and Aerospace Technology,* vol. 77, no. 1, pp. 34-41, 2005.

[67] B. Dix, "Aerofoil machining and polishing combined into a single automated process," *Int J Aircr Eng Aerosp Technol,* vol. 76, no. 5, 2004.

[68] G. G. Slabaugh, "Computing Euler angles from a rotation matrix," *Retrieved on August,* vol. 6, no. 2000, pp. 39-63, 1999.

[69] T. Kitagawa, A. Kubo, and K. Maekawa, "Temperature and wear of cutting tools in high-speed machining of Inconel 718 and Ti6Al6V2Sn," *Wear,* vol. 202, no. 2, pp. 142-148, 1997.

[70] *Autodesk PowerMill.* Available: https://www.autodesk.com/products/powermill/overview

[71] A. Sharman, R. C. Dewes, and D. K. Aspinwall, "Tool life when high speed ball nose end milling Inconel 718™," *Journal of Materials Processing Technology,* vol. 118, no. 1, pp. 29-35, 2001.

[72] "Master Catalog 2018," vol. Two: Rotating Tools, ed: Kennemetal Inc., 2017, pp. P112-P113.